



Vinicius Oliveira Fontes

**Topology optimization of hyperelastic
structures based on interpolation methods**

DISSERTAÇÃO DE MESTRADO

Dissertation presented to the Programa de Pós-Graduação em Engenharia Mecânica of PUC-Rio in partial fulfillment of the requirements for the degree of Mestre em Engenharia Mecânica.

Advisor: Prof. Anderson Pereira

Rio de Janeiro
September 2020



Vinicius Oliveira Fontes

**Topology optimization of hyperelastic
structures based on interpolation methods**

Dissertation presented to the Programa de Pós-Graduação em Engenharia Mecânica of PUC-Rio in partial fulfillment of the requirements for the degree of Mestre em Engenharia Mecânica. Approved by the Examination Committee.

Prof. Anderson Pereira

Advisor

Departamento de Engenharia Mecânica – PUC-Rio

Prof. Marco Antonio Meggiolaro

Departamento de Engenharia Mecânica – PUC-Rio

Prof. Pablo Andrés Muñoz Rojas

Departamento de Engenharia Mecânica – UDESC

Rio de Janeiro, September 30th, 2020

All rights reserved.

Vinicius Oliveira Fontes

The author received a bachelor's degree in Mechanical Engineering from Universidade Federal Fluminense (UFF) in 2018.

Bibliographic data

Fontes, Vinicius Oliveira

Topology optimization of hyperelastic structures based on interpolation methods / Vinicius Oliveira Fontes; advisor: Anderson Pereira – 2020.

88 f.: il. color.; 30 cm

Dissertação de Mestrado – Pontifícia Universidade Católica do Rio de Janeiro, Departamento de Engenharia Mecânica, 2020.

Inclui bibliografia

1. Engenharia Mecânica – Teses. Otimização topológica; Não-linearidade geométrica; Elementos finitos; Método de interpolação; Instabilidade numérica. I. Pereira, Anderson. II. Pontifícia Universidade Católica do Rio de Janeiro. Departamento de Engenharia Mecânica. III. Título.

CDD: 621

To Larissa, Vânia and Virginia.

Acknowledgments

First of all, I thank the Triune God for the opportunity to study and research in such a prestigious institution, under the guidance of many esteemed professors. I thank my family for their support throughout the years I studied in PUC-Rio, especially my grandparents.

I acknowledge the constant support of my advisor Anderson and my colleague and friend André, among others in my research group, without whom the present work would not be possible. The support from the university's staff is also acknowledged, especially those in the Department of Mechanical Engineering.

This study was financed in part by the Coordenação de Aperfeiçoamento de Pessoal de Nível Superior - Brasil (CAPES)¹ - Finance Code 001.

I also thank professor Krister Svanberg for sharing the MMA code used in this work.

¹Coordination for the Improvement of Higher Education Personnel.

Abstract

Fontes, Vinicius Oliveira; Pereira, Anderson (Advisor). **Topology optimization of hyperelastic structures based on interpolation methods**. Rio de Janeiro, 2020. 88p. Dissertação de Mestrado — Departamento de Engenharia Mecânica, Pontifícia Universidade Católica do Rio de Janeiro.

The optimized design of structures considering nonlinearities has been widely researched in the recent decades. The finite element analysis applied to topology optimization is jeopardized by the excessive deformation of low-density elements under high compression, which hinders the process of finding an optimal solution. Two methods, the Energy Interpolation scheme and the Additive Hyperelasticity technique, are implemented to overcome this difficulty in the minimum compliance problem, and hyperelastic material models are used to investigate their influence on the optimized topology. The Method of Moving Asymptotes is used to update the design variables whose sensitivities were calculated from the adjoint method. The state equation is solved through the Newton-Raphson method with an adjusting load step to reduce computational cost. Results for two benchmark problems are compared with those already established in the literature. The use of different hyperelastic models presented little influence on the final design of the structure. The Energy Interpolation method was able to converge for much higher loads than the default method, while the Additive Hyperelasticity presented convergence difficulties in plane strain.

Keywords

Topology Optimization; Geometrical Nonlinearity; Finite Elements; Energy Interpolation; Additive Hyperelasticity;

Resumo

Fontes, Vinicius Oliveira; Pereira, Anderson (Orientador). **Otimização topológica de estruturas hiperelásticas baseada em métodos de interpolação**. Rio de Janeiro, 2020. 88p. Dissertação de Mestrado — Departamento de Engenharia Mecânica, Pontifícia Universidade Católica do Rio de Janeiro.

O design otimizado de estruturas considerando não-linearidades tem sido amplamente pesquisado nas décadas recentes. A análise de elementos finitos aplicada à otimização topológica é prejudicada pela deformação excessiva de elementos de baixa densidade sob alta compressão, o que impede o processo de encontrar uma solução ótima. Dois métodos, o esquema Interpolação de Energia e a técnica de Hiperelasticidade Aditiva, são implementados para superar essa dificuldade no problema de minimização da flexibilidade, e modelos de materiais hiperelásticos são usados para investigar suas influências na topologia otimizada. O Método das Assíntotas Móveis é usado para atualizar as variáveis de projeto cujas sensibilidades foram calculadas pelo método adjunto. A equação de estado é resolvida através do método de Newton-Raphson com um incremento de carga ajustável para reduzir o custo computacional. Resultados de dois problemas de referência são comparados com aqueles já estabelecidos na literatura. O uso de diferentes modelos hiperelásticos apresentou pouca influência no design final da estrutura. O método de Interpolação de Energia foi capaz de convergir para cargas muito maiores que o método padrão, enquanto a Hiperelasticidade Aditiva apresentou dificuldades de convergência em estado plano de deformação.

Palavras-chave

Otimização Topológica; Não-linearidade Geométrica; Elementos Finitos; Interpolação de Energia; Hiperelasticidade Aditiva;

Contents

1	Introduction	18
1.1	Motivation	20
1.2	Literature Review	21
1.3	Objectives	27
1.4	Chapter index	27
2	Fundamentals of the Finite Element Method	28
2.1	Basics of Continuum Mechanics	28
2.1.1	Kinematics of Deformation	29
2.1.2	Stress Measures	29
2.1.3	Hyperelasticity	31
2.1.4	Compressibility formulations	33
2.2	Hyperelastic Material Models	35
2.3	Finite Element Equations	38
2.3.1	Cook's membrane problem	40
3	Topology Optimization	44
3.1	Optimization algorithm	46
3.1.1	Filtering	47
3.1.2	Projection and Penalization	49
3.2	Interpolation methods	51
3.2.1	No interpolation (None)	53
3.2.2	Energy Interpolation (EI)	54
3.2.3	Additive Hyperelasticity (AH)	55
3.2.3.1	Additive Hyperelasticity parameters	57
3.2.3.2	C-shape example	59
3.2.4	Comparison of the interpolation methods	61
3.3	Sensitivity Analysis	64
3.3.1	No interpolation (None)	66
3.3.2	Energy Interpolation	67
3.3.3	Additive Hyperelasticity	68
3.3.4	Validation of the sensitivity	68
4	Results and discussions	71
4.1	Comparison of hyperelastic models	72
4.2	Comparison of interpolation methods	76
4.3	Clamped beam	79
4.4	Final remarks	80
5	Conclusion	81
5.1	Suggestions for future works	82
5.1.1	Update scheme for Additive Hyperelasticity in plane strain	82
	Bibliography	84

List of Figures

1.1	Types of structural optimization (Bendsøe & Sigmund, 2002).	18
1.2	Optimized cantilever beam (Bendsøe, 1989).	19
1.3	Examples of optimized 3D printed designs.	20
1.4	Representation of nodes surrounded by void elements (Buhl <i>et al.</i> , 2000).	22
1.5	Mesh of an optimized beam with and without element removal (Bruns & Tortorelli, 2003).	22
1.6	Artificial zero-length link penalization (Yoon & Kim, 2005).	23
1.7	Influence of material models on the deformation of a C-shaped structure with a void region composed by low-density elements in gray (Lahuerta <i>et al.</i> , 2013).	24
1.8	Deformed C-shaped structure with the low-density elements (in white) modeled after two different formulations (Wang <i>et al.</i> , 2014).	25
2.1	Strain energy density and first principal Cauchy stress curves for different models in uniaxial deformation. Similar behavior is observed in the light gray region.	37
2.2	Cook's membrane problem (units in mm).	41
2.3	Vertical displacement (in millimeters) of the reference node for nH based models.	42
2.4	Vertical displacement (in millimeters) of the reference node for SVK based materials and Ansys' default model.	43
3.1	Design domain of a TO problem (Leitão & Pereira, 2019, adapted).	44
3.2	Design variable, filtered, projected and penalized.	47
3.3	Variation of optimal result as a function of refinement of the mesh for the MBB beam (Bendsøe & Sigmund, 2002, adapted).	47
3.4	Linear filter (Leitão & Pereira, 2019, adapted).	49
3.5	Smoothed Heaviside projection ($\eta = 0.5$) for different values of β .	50
3.6	Penalization of the projected variable for different values of p .	51
3.7	C-shape problem domain (units in mm) (Luo <i>et al.</i> , 2015, adapted).	51
3.8	C-shape domain using Q4 elements (dark gray: solid elements; light gray: low-density elements).	52
3.9	Interpolation parameter's projection for different values of p .	55
3.10	Schematic representation of the AH method (Luo <i>et al.</i> , 2015, adapted)	57
3.11	Stress-stretch curves for Yeoh models with different values of A_{20} and compressibility formulations.	58
3.12	Deformed mesh for the C-shape problem. Undeformed mesh in lighter shades of gray.	60
3.13	Compliance of the C-shape for different values of A_{20} (total NR iterations indicated).	61
3.14	Second C-shape problem domain adapted from Wang <i>et al.</i> (2014) (units in m).	61

3.15	Deformed mesh for the second C-shape problem. Undeformed mesh in lighter shades of gray.	62
3.16	Deformed mesh for the second C-shape problem using AH with $D_1 = 2/K$. Undeformed mesh in lighter shades of gray.	63
3.17	Clamped beam subject to a point load.	69
4.1	Cantilever beam domain, dimensions in meters (Leitão & Pereira, 2019, adapted).	72
4.2	Deformed mesh of the optimized cantilever beam using EI from different authors.	73
4.3	Undesirable topologies obtained at $\beta = 64$. V/V_Ω in parenthesis.	74
4.4	Optimized cantilever beam using Mooney-Rivlin and Yeoh models and their compliances. V/V_Ω in parenthesis.	76
4.5	Deformed optimized cantilever beam for $P = 144$ kN with different interpolation methods. End-compliance values in parenthesis.	77
4.6	Deformed optimized cantilever beam for $P = 500$ kN using EI and W^1 . End-compliance values in parenthesis.	78
4.7	Clamped beam domain, dimensions in meters (Leitão & Pereira, 2019, adapted).	79
4.8	Optimized topology for $P = 50$ kN using two interpolation methods. End-compliance and V/V_Ω in parenthesis.	79
4.9	Optimized topology for $P = 230$ kN with different interpolation methods. W^1 in plane strain was used in every case. End-compliance values in parenthesis.	80

List of Tables

1.1	Methods for dealing with numerical instabilities in TO.	26
2.1	Material models	35
2.2	u_y for SVK and nH materials.	42
3.1	Model of the void region for each interpolation methods.	53
3.2	Models used with the AH interpolation by different authors.	56
3.3	Parameters of the additive Yeoh material by different authors.	59
3.4	Results of the second C-shape problem using a step size of .05	63
3.5	Results of the second C-shape problem using a step size of 1.0	63
3.6	Parameters of the clamped beam problem	69
3.7	Numerical sensitivity analysis for the interpolation methods	70
4.1	Comparison of optimized topologies for models that use Jacobian terms added to the base SVK and nH. V/V_Ω in parenthesis.	73
4.2	Deformed structures for models that use Jacobian terms added to SVK and nH using the topology from Figure 4.2(c). $V/V_\Omega = 49.2\%$ for every case.	75
4.3	Performance of interpolation methods for the results shown in Figures 4.5(a) to 4.5(c).	78

List of Abbreviations

AH	Additive Hyperelasticity technique
APDL	ANSYS® Parametric Design Language
CFD	Central Finite Differences
EI	Energy Interpolation scheme
FEA	Finite Element Analysis
FEM	Finite Element Method
GNL	Geometrically Nonlinear
MEMS	Micro ElectroMechanical Systems
MIST	Moving Iso-Surface Threshold
MMA	Method of Moving Asymptotes
MR	Mooney-Rivlin (material model)
nH	neo-Hookean (material model)
NR	Newton-Raphson (convergence method)
OC	Optimality Criteria (optimization method)
Q4	4-node quadrilateral element
Q8	8-node quadrilateral element
RI	Residual Interpolation scheme
SEM	Super Element Method
SIMP	Solid Isotropic Material with Penalization
SVK	St. Venant-Kirchhoff (material model)
TO	Topology Optimization

List of Symbols

Math Operators

$\nabla_0(\bullet)$	Gradient operator with respect to the reference configuration of the body
$\text{tr}(\bullet)$	Trace operator
$\det(\bullet)$	Determinant
\cdot	Dot product
$:$	Contraction operator (double dot)
\cap	Assembly operator

Continuum Mechanics

d	Displacement field
I	Identity matrix
F	Deformation gradient tensor
J	Jacobian of the deformation
C	Right Cauchy-Green deformation tensor
E	Green-Lagrange strain tensor
ε	Small strain tensor
σ	Cauchy stress tensor
P	1st Piola-Kirchhoff stress tensor (PK1)
S	2nd Piola-Kirchhoff stress tensor (PK2)

Hyperelasticity

W	Strain energy density
W_{vol}	Strain energy density: volumetric dilation term
W_{iso}	Strain energy density: isochoric (distortional) term
W_J	Strain energy density: Jacobian term

W^L	Strain energy density of linear model (from small deformation theory)
W^{NL}	Strain energy density of a nonlinear hyperelastic model
λ_i	Principal stretches (eigenvalues of \mathbf{F})
I_i	Principal invariants of \mathbf{C}
J_i	Reduced invariants of \mathbf{C}
A_{mnk}	Constants of a generic hyperelastic material
A_{mn}	Constants of a nearly incompressible hyperelastic material
\mathbf{D}	Constitutive tensor
E	Young modulus
ν	Poisson coefficient
λ	Lamé's first parameter
μ	Lamé's second parameter (shear modulus)
K	Bulk modulus
D_i	Compressibility constants

Finite Element Method

Π	Total potential energy
Π^{int}	Stored (internal) strain energy
Π^{ext}	Work done by external forces
$\delta\Pi$	First variation of the total potential energy
$\bar{\mathbf{d}}$	First variation of the displacement
a	Energy form
l	Load form
\mathbf{u}	Nodal displacement vector (global scope)
$\Delta\mathbf{u}$	Increment of nodal displacement vector (global scope)
\mathbf{r}	Residual vector (global scope)
\mathbf{f}_{int}	Internal force vector (global scope)
\mathbf{f}_{ext}	External force vector (global scope)
\mathbf{K}_T	Tangent stiffness matrix (global scope)
\mathbf{u}_e	Nodal displacement (element scope)

W_e	Strain energy density (element scope)
\mathbf{f}_e	Internal force vector (element scope)
\mathbf{K}_e	Tangent stiffness matrix (element scope)
\mathbf{B}_G	Linear (geometric) strain–displacement matrix
\mathbf{B}_N	Nonlinear strain-displacement matrix
Ω_e^0	Undeformed configuration of element e

Geometry and Loads

L	Length
H	Height
t	Thickness
$\mathbf{P}, \mathbf{f}_1, \mathbf{f}_2$	Applied force vector
P, f_1, f_2	Applied force magnitude

Topology Optimization

Ω	Design domain
Ω_S	Design domain (solid region)
Ω_V	Design domain (void region)
$\partial\Omega$	Boundary of Ω
Γ_D	Boundary with displacement boundary conditions
Γ_N	Boundary with traction (natural) boundary conditions
\mathbf{x}	Design variable vector
$\tilde{\mathbf{x}}$	Filtered variable vector
$\bar{\mathbf{x}}$	Projected variable vector
$\hat{\mathbf{x}}$	Penalized variable vector
Δx_{lim}	Maximum change of \mathbf{x} per iteration of TO (move limit)
c	End-compliance
V	Current volume of the structure
V_e	Volume of element e
V_Ω	Volume of the domain Ω

V_{frac}	Maximum volume fraction allowed in the optimized structure
a_i, c_i, d_i	Constants used in the MMA
y_i, z	Artificial variables used in the MMA
$w_{e,i}$	i -th weight associated with element e
$d_{e,i}$	Distance between the centroids of the elements e and i
\mathbf{M}	Filter matrix
β	Sharpness parameter of the projection
η	Threshold variable of the projection
ϵ	Lower-boundary of the element density (Ersatz parameter)
p	Penalization factor
Δp	Increment of the penalization factor
$W_e^L, \mathbf{f}_e^L, \mathbf{K}_e^L$	Strain energy density, internal force vector and tangent stiffness matrix of the linear material (from small deformation theory)
$W_e^{NL}, \mathbf{f}_e^{NL}, \mathbf{K}_e^{NL}$	Strain energy density, internal force vector and tangent stiffness matrix of a nonlinear material
$W_e^Y, \mathbf{f}_e^Y, \mathbf{K}_e^Y$	Strain energy density, internal force vector and tangent stiffness matrix of the added Yeoh material
γ_e	Interpolation factor of element e
β_1	Sharpness parameter of the energy interpolation method
ρ_0	Threshold variable of the energy interpolation method
$E_{\text{von}}^{(k)}$	Maximal von Mises equivalent strain at TO iteration k
E^*	Reference strain
E_e^{dev}	Strain tensor of element e (deviatoric part)
E_e^{GP}	Strain tensor of element e (average of the components evaluated at Gauss points of element e)
λ	Adjoint vector
λ_e	Adjoint vector (only the components associated with the degrees of freedom of element e)

*For You will not abandon my soul to Hades, nor
will You allow Your Holy One to see corruption.*

Peter.
Acts 2:27 (MEV).

1

Introduction

The analysis of structures is based on solving differential equations that often are difficult or impossible to do analytically. The advent of the digital computer has given effectiveness and applicability in solving these problems with the Finite Element Analysis (FEA) which, due to its practical implementation, “found wide appeal in engineering practice” (Bathe, 2014). In the same fashion, other fields of interest in engineering have risen since the past century, such as numerical optimization. These fields of research combined lead to the study of structural optimization, which is often divided in three types: sizing, shape and topology optimization (Figure 1.1).

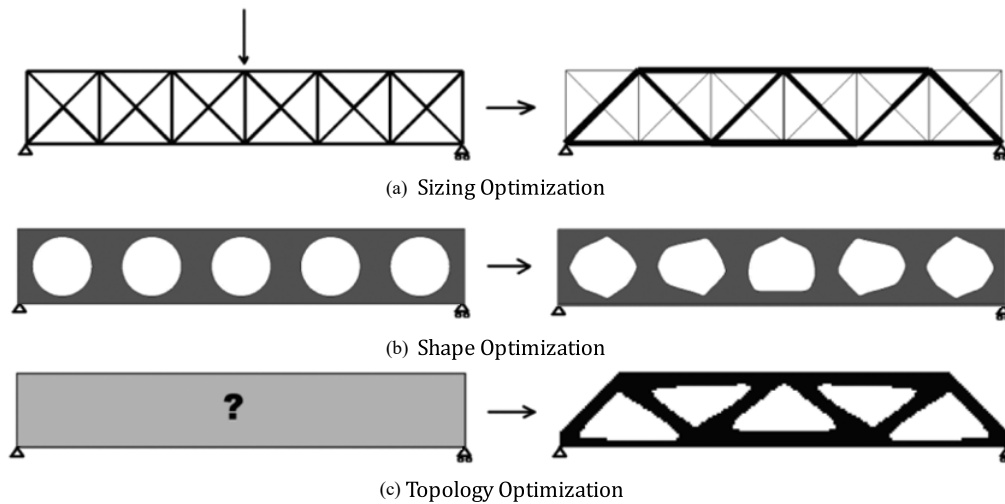


Figure 1.1: Types of structural optimization (Bendsøe & Sigmund, 2002).

Sizing optimization aims to find the optimal structural parameters in an already known structure (*e.g.*, thickness of members in a truss, see Figure 1.1a); shape optimization seeks to find the optimal boundary shape of a domain with an already known topology (*e.g.*, the holes in a beam, see Figure 1.1b); topology optimization (TO) involves determining the optimal distribution of material in a given domain (*e.g.*, material layout of a beam, see Figure 1.1c). In topology optimization, the only information known is the boundary conditions (loads and supports, for the purposes of this text) and the desired volume of

material in a previously chosen domain which may or may not include fixed solid and void regions (Bendsøe & Sigmund, 2002).

When it was first introduced by Bendsøe & Kikuchi (1988) with the homogenization method, topology optimization was implemented using linear finite elements in order to solve the minimum compliance problem (*i.e.*, to find the topology that minimizes the work of the external forces). Bendsøe (1989) later introduced the approach known as Solid Isotropic Material with Penalization (SIMP) where a penalized continuous design variable would serve to determine the existence of material (or lack thereof) in a chosen domain. This continuous variable x_e , often called element density, is used to change the stiffness of each element that composes the domain of a structure to be optimized, such that an element e is solid when $x_e = 1$ and void (or nonexistent) when $x_e = 0$. One of the first published results for the cantilever beam using this method is shown in Figure 1.2, a problem that has been revisited by many authors in the following decades.



Figure 1.2: Optimized cantilever beam (Bendsøe, 1989).

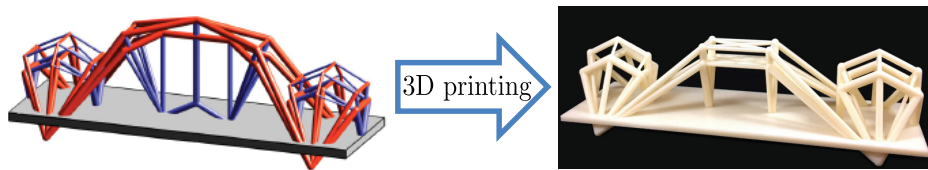
The SIMP method helps recover the discrete nature of the original problem, since x_e might assume any value within the continuous range $[0, 1]$ during the TO process, a requirement for using gradient-based optimization. When a convergence criterion is met, some post-processing of the optimized design may be required to comply with necessary restrictions, such as manufacturing limitations.

Although intermediate values of density x_e may be physically meaningful for composite materials, *e.g.*, in the work by Huang *et al.* (2013), in many cases (such as this work), only the 0 and 1 values are desirable at the end of the TO process. Therefore, the set of low-density elements in the mesh, often referred to as “void region” by some authors, is disregarded in the optimized design.

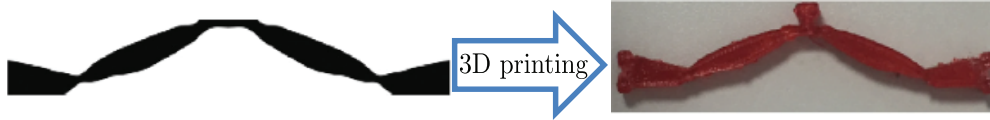
1.1

Motivation

Many TO applications, such as the first works in the area, consider linear analysis that assume small displacements and linear elastic material. However, when structures deform past a limit, such assumptions may not be valid, as it is expected for soft or slender structures and mechanisms (Bendsøe & Sigmund, 2002). For instance, the high aspect ratio of flexible wings in modern aircraft deforms enough to require nonlinear formulation for its analysis, as observed by Jie *et al.* (2020) and references therein.



1.3(a): Suspension bridge considering material nonlinearities (adapted from Zhang *et al.* (2017)).



1.3(b): Bistable mechanism considering material and geometric nonlinearities (adapted from Chen *et al.* (2019b)).

Figure 1.3: Examples of optimized 3D printed designs.

Many authors have explored the intricacies of the TO applications to additive manufacturing (also referred to as 3D printing), where the linear framework may be unsuitable, thus more robust methods have been explored: Zhang *et al.* (2017) optimized the trusses that support a suspension bridge using the ground structure method, considering material nonlinearities (see Figure 1.3(a)); James & Waisman (2016) and Chen *et al.* (2019b) designed a structure with two stable equilibrium positions known as a bistable mechanism (see Figure 1.3(b)), where both material and geometric nonlinearities are fundamental in the analysis. For a more comprehensive review on TO and additive manufacturing, the reader is referred to Liu *et al.* (2018).

Nonlinear TO has also been successfully applied to the design of Micro-ElectroMechanical Systems (MEMS) and compliant mechanisms in general, structures optimized to maximize displacement rather than minimizing structural compliance. Although early works such as Frecker *et al.* (1997) have considered a linear setting, others have optimized compliant mechanisms undergoing large displacement, such as Bruns & Tortorelli (1998); Pedersen *et al.*

(2001); Lazarov *et al.* (2011), which is intrinsic to their application. The use of hyperelastic material models, which are often applied to polymers, may also be used to model metallic compliant mechanisms and other structures that undergo large displacements.

The difficulty in working with geometrically non-linear (GNL) TO is due to the behavior of low-density elements under large deformation. Even if the void region is fictitious and disregarded in the end design, it may still significantly affect the FEA and jeopardize convergence when higher loads are considered. Although many solutions to this problem have been suggested in the literature, it is still being investigated by many authors as presented in the next section. It is noted that this work is motivated by the suggestions of the master thesis by Leitão (2019), from which a substantial part of the terminology and implementation derived.

1.2

Literature Review

The fields of study that compose this work can be divided into three main parts: structural analysis, sensitivity analysis and topology optimization. This section is dedicated to reviewing the solutions for numerical instabilities in the structural analysis of nonlinear TO.

Early works by Bruns & Tortorelli (1998), Buhl *et al.* (2000) and others considered the use of a total Lagrangian formulation in GNL TO in order to investigate the optimized designs of structures under large displacements that depend on the applied load, unlike its linear counterpart. It is well-known in the literature that FEA convergence is particularly difficult when low-density elements are subject to large deformation. One cause of this problem is the loss of the positive definite property of the stiffness matrix for elements under excessive deformation. It is worthy of note that the use of robust solution techniques such as the arc-length method (ALM) described by Crisfield (1981) does not guarantee convergence. Some solutions to this problem have been proposed and are outlined in the following paragraphs.

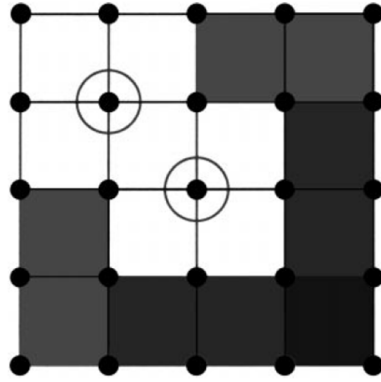
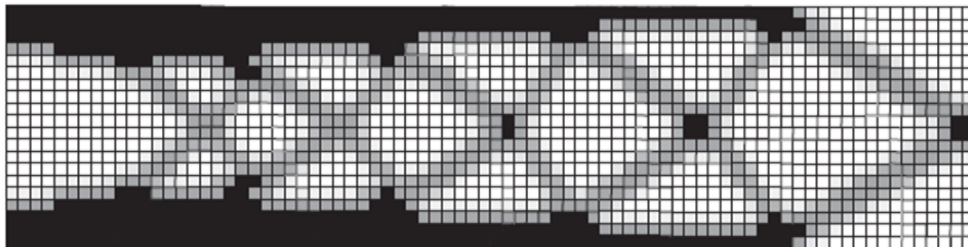
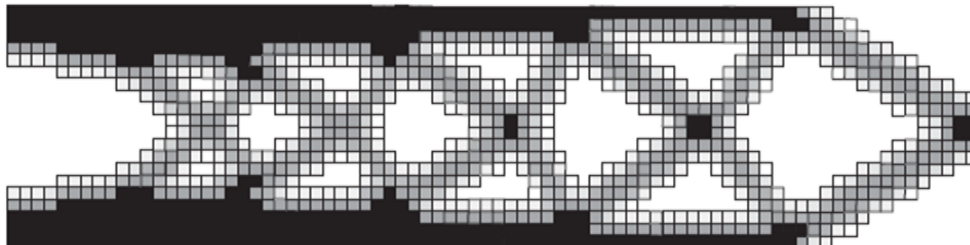


Figure 1.4: Representation of nodes surrounded by void elements (Buhl *et al.*, 2000).

Buhl *et al.* (2000) first proposed to remove nodes surrounded by void elements from the convergence criterion, but not from the mesh itself (see Figure 1.4). Bruns & Tortorelli (2003) removed and reintroduced elements from the mesh using a mesh-independent Gaussian weighted discrete filter, whose application is shown in Figure 1.5 for the cantilever beam problem. Luo & Tong (2016) also proposed the removal of void elements from FEA but considered them for the response function. Applying the Moving Iso-Surface Threshold (MIST) method allowed removed elements to be considered in the design variable update, reappearing when needed.



1.5(a): Without element removal.



1.5(b): With element removal.

Figure 1.5: Mesh of an optimized beam with and without element removal (Bruns & Tortorelli, 2003).

Yoon & Kim (2005) penalized artificial zero-length elastic links that connected the elements, instead of penalizing each element's stiffness, as shown in Figure 1.6. Kawamoto (2009) implemented the Levenberg-Marquardt to achieve convergence of the FEA during TO of compliant mechanisms.

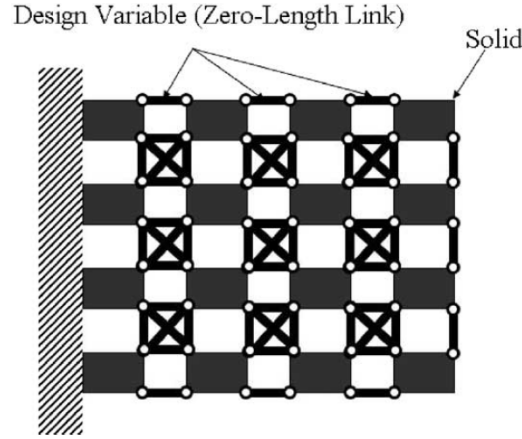
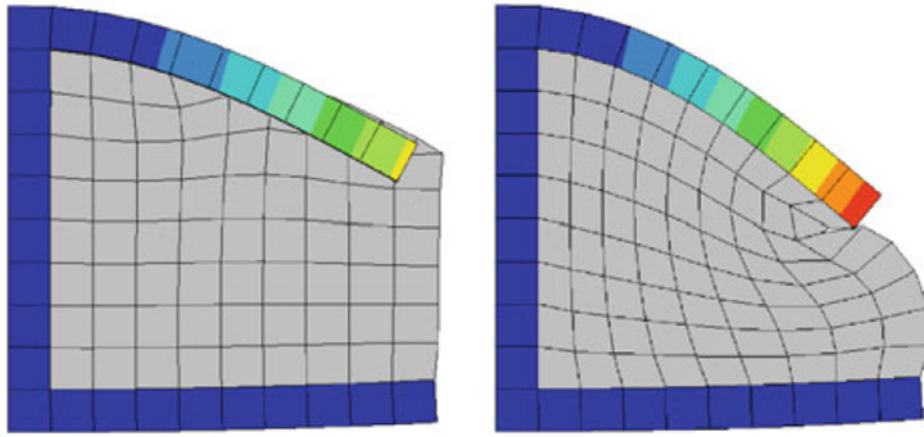


Figure 1.6: Artificial zero-length link penalization (Yoon & Kim, 2005).

Lahuerta *et al.* (2013) provided an important discussion of the use of polyconvex materials along a relaxation filter to avoid the loss of ellipticity. They compared the deformation of the void region of a C-shaped structure formulated with the conventional St.Venant-Kirchhoff (SVK) model and an enhanced polyconvex neo-Hookean (nH) model. Figure 1.7 shows that the former presents a undesirable stiffer response compared to the latter. Further discussion of the importance of polyconvexity for hyperelasticity in FEA is provided by Suchocki & Jemioło (2019) and references therein. Klarbring & Strömberg (2013) also proposed the use of different hyperelastic material models in TO, while also considering prescribed displacement.



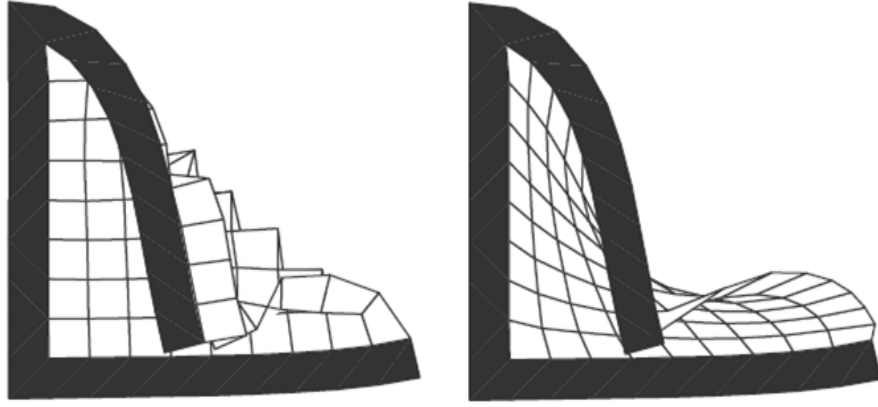
1.7(a): St.Venant-Kirchhoff.

1.7(b): neo-Hookean of Simo-Ciarlet.

Figure 1.7: Influence of material models on the deformation of a C-shaped structure with a void region composed by low-density elements in gray (Lahuerta *et al.*, 2013).

van Dijk *et al.* (2014) have shown that the Green-Lagrange strain measure is problematic due to the loss of its physical meaning under compression. The proposed solution was to scale the displacement of low-density elements to maintain them in their applicable range.

Few authors have proposed to interpolate the energy function for each element to alleviate numerical instabilities. Depending on its density, each element would be modeled after either the original model (for solid regions) or a “soft” model (for void regions). Wang *et al.* (2014) suggested using small deformation theory for the soft material. Figure 1.8 shows another deformed C-shaped structure, where it is seen that modeling only the low-density elements with linear elements from small deformation theory results in a less distorted mesh.



1.8(a): Using nonlinear elements. 1.8(b): Using small deformation theory.

Figure 1.8: Deformed C-shaped structure with the low-density elements (in white) modeled after two different formulations (Wang *et al.*, 2014).

Some authors were influenced by this work and have made modifications to the original idea in order to improve its performance: Wallin *et al.* (2018) slightly altered the transition parameter to a continuous one and used a neo-Hookean material; Jie *et al.* (2020) adapted the Super Element Method (SEM) to consider elements with density below a given threshold as a single macro-element confined to linear elastic deformation.

Luo *et al.* (2015) proposed interpolating the energy with the Yeoh model, which was later implemented by Chen *et al.* (2019a) using Ansys with a slightly different model.

Table 1.1 displays the previously presented methods in chronological order. To the best of this author's knowledge, there have been no efforts to compare different interpolation methods in plane strain assumption in TO. The main goal of this thesis is to develop a MATLAB code for topology optimization with support for material and geometrical nonlinearities, as discussed in the following section. The code was written based on the implementation by Leitão & Pereira (2019) and with the help of their authors.

Table 1.1: Methods for dealing with numerical instabilities in TO.

Year	Authors	Method
2000	Buhl, T. Pedersen, C. B. W. Sigmund, O.	Relaxing Convergence Criterion
2003	Bruns, T.E Tortorelli, D. A.	Element removal and reintroduction
2005	Yoon, H. G. Kim, Y. Y.	Element connectivity parametrization
2009	Kawamoto, A.	Levenberg-Marquardt method
2012	Lee, H. Park, G.	Equivalent Static Load Method
2013	Lahuerta, R. D. Simões, E. T. Campello, E. M. B. Pimenta, P. M. Silva, E. C. N.	Use of polyconvex material models
2014	van Dijk, N. P. Langelaar M. van Keulen, F.	Element deformation scaling
2014	Wang, F. Lazarov, B. S. Sigmund, O. Jensen, J. S.	Energy Interpolation Scheme
2015	Luo, Y. Wang, M. Y. Kang, Z.	Additive hyperelasticity technique
2016	Luo, Q. Tong, L.	Moving iso-surface threshold
2018	Wallin, M. Ivarsson, N. Tortorelli, D.	Modified Energy Interpolation scheme
2019	Chen, Q. Zhang, X. Zhu, B.	Additive hyperelasticity technique
2020	Hou, J. Gu, X. Zhu, J. Wang, J. Zhang, W.	Super Elements Method

1.3

Objectives

A complete TO code including the FEA was written on MATLAB to achieve the following goals:

1. Compare the optimized topology obtained using several hyperelastic material models;
2. Compare the applicability of two interpolation methods (Additive Hyperelasticity technique and Energy Interpolation scheme) to problems in plane strain condition.

All problems in this work are analyzed assuming plane strain condition, unless otherwise stated. Some adaptations to the original interpolation methods were adopted in order to both provide a fair comparison and to enable the use of the aforementioned hyperelastic models.

1.4

Chapter index

The topics discussed in this thesis are divided as follows:

Chapter 2 is a brief review on fundamental concepts and equations from hyperelasticity and FEA;

Chapter 3 introduces TO concepts and their implementation using interpolations;

Chapter 4 presents the results of two benchmark problems using various hyperelastic materials and two interpolation techniques;

Chapter 5 concludes the work and presents proposals for future works.

Some problems and results are shown throughout the following chapters to either better illustrate the topics or validate results.

2

Fundamentals of the Finite Element Method

This chapter is dedicated to describing basic notions and formulas for future reference in this text. The Finite Element Method (FEM) is a well-spread tool in engineering used to numerically solve partial-differential equations by dividing it into geometrical parts called finite elements whose behavior is approximated by simpler functions. Then, they are assembled into a system of algebraic equations that can be solved by any desirable method, often based on the Newton-Raphson (NR) method.

FEM equations can be derived using the Calculus of Variations and its application extends to many different fields other than structural analysis. Hence, a wider definition of FEM has been proposed as “a general discretization procedure of continuum problems posed by mathematically defined statements” (Zienkiewicz *et al.*, 2005).

This chapter starts by defining important concepts from Continuum Mechanics applied to finite elasticity. General remarks on the FEM are presented, along with by the definition of the hyperelastic models used in this thesis, which are illustrated by a problem solved with an FEA code written in MATLAB.

For the sake of conciseness, most proofs and derivations are avoided, so the reader is referred to Bonet & Wood (2008); Kim (2014); Bathe (2014) for further information.

2.1

Basics of Continuum Mechanics

Although matter is not continuous, the continuum theory assumes that it “may be divided indefinitely into smaller and smaller portions, each of which retains all of the physical properties of the parent body” (Mase *et al.*, 1999, p. 16).

The following equations can be formulated by taking either the initial or current configuration as a reference. The Lagrangian (or material) description assumes the former, while the Eulerian (or spatial) description assumes the latter. Material description is adopted unless otherwise stated.

2.1.1

Kinematics of Deformation

The deformation of a body may be computed from the displacement field \mathbf{d} by the deformation gradient \mathbf{F} , calculated from the equation

$$\mathbf{F} = \nabla_0 \mathbf{d} + \mathbf{I}, \quad (2.1)$$

where $\nabla_0 \mathbf{d}$ is the gradient of the displacement field \mathbf{d} and \mathbf{I} is the second order identity tensor. The 0 subscript enforces that the gradient is taken with respect to the initial configuration of the body. Another important measure, known as the right Cauchy-Green deformation tensor, is defined as

$$\mathbf{C} = \mathbf{F}^T \mathbf{F}. \quad (2.2)$$

An important measure known as the Green-Lagrange strain is computed from the following equation:

$$\mathbf{E} = \frac{1}{2}(\mathbf{C} - \mathbf{I}), \quad (2.3)$$

that can also be expressed in terms of the displacement as

$$\mathbf{E} = \frac{1}{2} \left[\nabla_0 \mathbf{d} + (\nabla_0 \mathbf{d})^T + (\nabla_0 \mathbf{d})^T \nabla_0 \mathbf{d} \right]. \quad (2.4)$$

When small strains are considered, the second order terms in (2.4) may be neglected. Thus, the small strain tensor is defined as

$$\boldsymbol{\varepsilon} = \frac{1}{2} \left[\nabla_0 \mathbf{d} + (\nabla_0 \mathbf{d})^T \right]. \quad (2.5)$$

2.1.2

Stress Measures

Stress is the ratio of internal force on a body per unit area, and can be defined in many ways. The Cauchy (or true) stress tensor $\boldsymbol{\sigma}$ is the ratio between the aforementioned quantities taken in the current configuration of the system. Moreso, from the conservation of angular momentum, it may be shown that $\boldsymbol{\sigma} = \boldsymbol{\sigma}^T$, *i.e.*, the Cauchy stress tensor is symmetric (Mase *et al.*, 1999).

Albeit physically meaningful, $\boldsymbol{\sigma}$ is defined in a spatial description. The first Piola-Kirchhoff tensor is defined through a procedure called pull-back, that yields

$$\mathbf{P} = J\boldsymbol{\sigma}\mathbf{F}^{-T}, \quad (2.6)$$

where

$$J = \det(\mathbf{F}) \quad (2.7)$$

is the Jacobian, a measure of volume change during deformation, such that $J = 1$ for an isochoric change. Unfortunately, \mathbf{P} is not a symmetric tensor. Thus the second Piola-Kirchhoff tensor, shortened to PK2, is defined as

$$\mathbf{S} = \mathbf{F}^{-1}\mathbf{P}, \quad (2.8)$$

which is symmetric. Although not physically meaningful, PK2 is a most useful stress measure for solid mechanics, and is more convenient for many numerical implementations. It is often necessary, however, to express the stress back in the current configuration, which can be done by solving (2.8) for $\boldsymbol{\sigma}$, that is

$$\boldsymbol{\sigma} = \frac{1}{J}\mathbf{F}\mathbf{S}\mathbf{F}^T. \quad (2.9)$$

When considering a body's behavior in two dimensions, there are two approximations often used to simplify the description. Let a plane be defined by directions 1 and 2, with 3 being the out-of-plane direction. Furthermore, assume that loading is applied only in plane 1-2.

Plane stress assumes that out-of-plane stress components are zero, that is

$$\sigma_{13} = \sigma_{31} = \sigma_{23} = \sigma_{32} = \sigma_{33} = 0. \quad (2.10)$$

This approximation is often assumed when a structure's thickness is much smaller than the other dimensions, e.g. a thin metal plate, where the stress across the thickness is negligible.

Plane strain assumes that out-of-plane strain components are zero, that is

$$E_{13} = E_{31} = E_{23} = E_{32} = E_{33} = 0. \quad (2.11)$$

Likewise, for small displacements,

$$\varepsilon_{13} = \varepsilon_{31} = \varepsilon_{23} = \varepsilon_{32} = \varepsilon_{33} = 0. \quad (2.12)$$

Plane strain is a fair assumption when displacement is constrained in one direction or if the thickness of a body is comparable to the other dimensions, such that strain in the out-of-plane direction is negligible.

2.1.3

Hyperelasticity

A hyperelastic material is defined by a functional that depends solely on its current strain state, so it is not dependent on deformation history (Holzapfel, 2000). This functional measures the stored energy per unit volume in a body and is only a function of \mathbf{F} . For ease of reading, this text uses the term strain energy density instead, represented by the letter W . A measure of deformation such as \mathbf{C} and \mathbf{E} may also be used to define W , since they depend on \mathbf{F} .

Holzapfel (2000) derives stress and strain relationships for hyperelastic materials from the strain energy density, forming pairs known as work conjugates. The work conjugate of PK2 stress is the Green-Lagrange strain and their relationship is given by

$$\mathbf{S} = \frac{\partial W}{\partial \mathbf{E}}. \quad (2.13)$$

Isotropic materials are those whose properties do not depend on direction. The strain energy density of an isotropic material can be defined as a function of its strain's principal invariants, according to the representation theorem for tensor valued functions (Gurtin, 1981). This allows one to define the strain energy density as $W = W(I_1, I_2, I_3)$, where I_i are the principal invariants of \mathbf{C} , which is itself a function of \mathbf{F} . The invariants can be calculated from the principal stretches λ_i , that is

$$I_1 = \lambda_1^2 + \lambda_2^2 + \lambda_3^2, \quad (2.14)$$

$$I_2 = \lambda_1^2 \lambda_2^2 + \lambda_2^2 \lambda_3^2 + \lambda_3^2 \lambda_1^2, \quad (2.15)$$

$$I_3 = \lambda_1^2 \lambda_2^2 \lambda_3^2. \quad (2.16)$$

The principal invariants may be computed in terms of the right Cauchy-Green strain tensor instead:

$$I_1 = \text{tr}(\mathbf{C}), \quad (2.17)$$

$$I_2 = \frac{1}{2} [\text{tr}^2(\mathbf{C}) - \text{tr}(\mathbf{C}^2)], \quad (2.18)$$

$$I_3 = \det(\mathbf{C}). \quad (2.19)$$

A more convenient definition of PK2 is defined by substituting (2.3) into (2.13) and applying the chain rule that yields

$$\mathbf{S} = 2 \frac{\partial W}{\partial \mathbf{C}}. \quad (2.20)$$

Likewise, the constitutive tensor \mathbf{D} is defined as the partial derivative of \mathbf{S} with respect to \mathbf{E} . Repeating the same procedure as above for \mathbf{D} gives

$$\mathbf{D} = 2 \frac{\partial \mathbf{S}}{\partial \mathbf{C}}. \quad (2.21)$$

Other definitions of the strain energy density are found in the literature, such as defining it in terms of λ_i (useful for anisotropic materials) or as a function of \mathbf{E} . A useful definition is as follows:

$$W = \sum_{m+n+k=1}^{\infty} A_{mnk} (I_1 - 3)^m (I_2 - 3)^n (I_3 - 1)^k \quad (2.22)$$

where A_{mnk} are constants to be defined for each model and material. The first two invariants in (2.22) are subtracted by 3 to ensure their respective terms are null when strain is zero (Mase *et al.*, 1999). The third invariant is subtracted by 1 to nullify the terms that consider volumetric dilation during isochoric deformation (*i.e.*, $I_3 = J^2 = 1$).

Finally, many materials can be defined in terms of the Young modulus E and the Poisson coefficient ν taken from experimental data. On the other

hand, defining a material in terms of Lamé's parameters is useful in many implementations, which can be calculated from

$$\lambda = \frac{E\nu}{(1+\nu)(1-2\nu)}, \quad (2.23)$$

$$\mu = \frac{E}{2(1+\nu)} \quad (2.24)$$

where λ is Lamé's first parameter and μ is the second parameter, also known as the shear modulus. An important compressibility parameter is the bulk modulus, computed from Lamé's parameters by

$$K = \lambda + \frac{2}{3}\mu. \quad (2.25)$$

2.1.4

Compressibility formulations

Hyperelastic models are used to simulate the behavior of solids which usually show some degree of incompressibility. Notice that the formulations presented in Section 2.1.3 do *not* enforce incompressibility by default, and also may not realistically represent the physical behavior of a material under significant compression. Three types of compressibility formulations are often used to enhance these models and provide some resistance to the change of volume.

- Near incompressibility

A nearly incompressible material has its strain energy density separated into two parts: W_{vol} considers the effects of volumetric dilation and W_{iso} considers the effects of isochoric distortion, that is:

$$W(\mathbf{C}) = W_{vol}(J) + W_{iso}(J_1, J_2) \quad (2.26)$$

where J_1 and J_2 , known as the reduced invariants, do not depend on the effects of volumetric dilation and are defined as

$$J_1 = J^{-\frac{2}{3}} I_1, \quad (2.27)$$

$$J_2 = J^{-\frac{4}{3}} I_2. \quad (2.28)$$

Many commercial programs implement this formulation in two fashions. The first, known as the penalty method (Kim, 2014, p. 192-193):

$$W_{vol}(J) = \frac{K}{2}(J - 1)^2. \quad (2.29)$$

Near incompressible behavior is achieved by setting the bulk modulus to a high value, *e.g.*, $10^3\mu - 10^4\mu$ (Bonet & Wood, 2008, p. 171). Some material models are often implemented using a more complex version of this formulation by adding higher order terms, that is,

$$W_{vol}(J) = \sum_{n=1}^N \frac{1}{D_n} (J - 1)^2 \quad (2.30)$$

where D_n are compressibility constants. In order to agree with (2.29),

$$D_1 = \frac{2}{K}, \quad (2.31)$$

but other values may be used according to the application.

– Incompressibility

Incompressible behavior can be mathematically implemented with a Lagrange multiplier into (2.26) as follows:

$$W_{vol}(J) = p(J - 1), \quad (2.32)$$

where p physically represents a workless hydrostatic pressure, determined from the boundary conditions. Some degree of compressibility can be observed due to numerical approximations in computational implementations.

– Jacobian terms

Adding functions $W_J(J)$ to the strain energy density functional has been proposed in the literature, such as

$$W_J = \frac{1}{2}(\ln J)^2, \quad (2.33)$$

$$W_J = \lambda(J - \ln J - 1), \quad (2.34)$$

$$W_J = \frac{\lambda}{2}(J - 1)^2. \quad (2.35)$$

Equation (2.34) was suggested by Curnier (1994), but (2.33) and (2.35) were proposed by Klarbring & Strömberg (2013). The term

$$W_J(J) = -\mu \ln J \quad (2.36)$$

is also found in the literature applied to neo-Hookean models to give them resistance to compression.

2.2

Hyperelastic Material Models

Hyperelastic models are inspired by either a phenomenological description of a material behavior or from a mathematical representation of its micro structure. These aspects are not addressed in this text due to the focus being mainly their implementation in the FEA, so the reader is referred to Holzapfel (2000) and references therein for further information. It is possible, then, to implement the same material with different models, as is done in examples throughout this thesis.

Table 2.1 is a comprehensive list of the models used in this work, including the linear model W^L and the following hyperelastic models: St.Venant-Kirchhoff, neo-Hookean, Mooney-Rivlin (MR) and Yeoh.

Table 2.1: Material models

Model	Type	Formulation	Strain energy density
W^L	Linear [†]	-	$\frac{\lambda}{2}(\varepsilon_{kk})^2 + \mu\varepsilon_{ij}\varepsilon_{ij}$
W^1	SVK	-	$\frac{\lambda}{8}(I_1 - 3)^2 + \frac{\mu}{4}(I_1^2 - 2I_2 - 2I_1 + 3)$
W^2	SVK [‡]	(2.33)	$\frac{\lambda}{2}(\ln J)^2 + \frac{\mu}{4}(I_1^2 - 2I_2 - 2I_1 + 3)$
W^3		(2.34)	$\lambda(J - \ln J - 1) + \frac{\mu}{4}(I_1^2 - 2I_2 - 2I_1 + 3)$
W^4		(2.35)	$\frac{\lambda}{2}(J - 1)^2 + \frac{\mu}{4}(I_1^2 - 2I_2 - 2I_1 + 3)$
W^5	nH [‡]	(2.33)	$\frac{\lambda}{2}(\ln J)^2 - \mu \ln J + \frac{\mu}{2}(I_1 - 3)$
W^6		(2.34)	$\lambda(J - \ln J - 1) - \mu \ln J + \frac{\mu}{2}(I_1 - 3)$
W^7		(2.35)	$\frac{\lambda}{2}(J - 1)^2 - \mu \ln J + \frac{\mu}{2}(I_1 - 3)$
W^8	MR	(2.29)	$A_{10}(J_1 - 3) + A_{01}(J_2 - 3) + \frac{K}{2}(J - 1)^2$
W^9	Yeoh	(2.30)	$\sum_{m=1}^3 A_{m0}(J_1 - 3)^m + \sum_{n=1}^N \frac{1}{D_n}(J - 1)^{2n}$

[†] Linear model from small deformation theory;

[‡] Modified versions proposed by Curnier (1994) and Klarbring & Strömberg (2013).

The linear model W^L from small deformation theory is defined in terms of the linearized strain ϵ , a linear function of the displacements (*cf.* (2.5)). The column **Formulation** lists the compressibility formulation of each model as presented in Section 2.1.4, when there is one.

From consistency conditions, the constants A_{10} and A_{01} can be determined in terms of μ from the following equation (Kim, 2014, p. 189):

$$A_{10} + A_{01} = \frac{\mu}{2}. \quad (2.37)$$

The tensors \mathbf{S} and \mathbf{D} were calculated from (2.20) and (2.21) using MATLAB's Symbolic Math Toolbox, with the exception of W^L , whose equations can be readily found in FEM literature, *e.g.*, Kim (2014).

Plane strain is assumed in every problem in this work unless otherwise stated. This condition can be enforced by first solving (2.3) for \mathbf{C} :

$$\mathbf{C} = 2\mathbf{E} + \mathbf{I}. \quad (2.38)$$

Then, substituting (2.11) into (2.38) in matrix form gives

$$\begin{bmatrix} C_{11} & C_{12} & C_{13} \\ C_{12} & C_{22} & C_{23} \\ C_{13} & C_{23} & C_{33} \end{bmatrix} = 2 \begin{bmatrix} E_{11} & E_{12} & 0 \\ E_{12} & E_{22} & 0 \\ 0 & 0 & 0 \end{bmatrix} + \begin{bmatrix} 1 & 0 & 0 \\ 0 & 1 & 0 \\ 0 & 0 & 1 \end{bmatrix}. \quad (2.39)$$

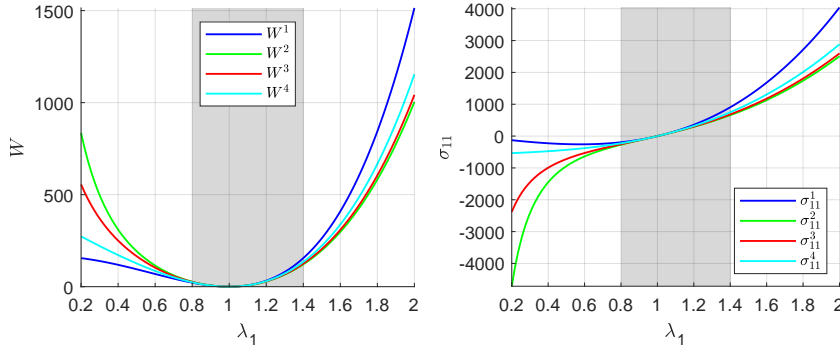
The deformation tensor should be defined as

$$\mathbf{C} = \begin{bmatrix} C_{11} & C_{12} & 0 \\ C_{12} & C_{22} & 0 \\ 0 & 0 & 1 \end{bmatrix}. \quad (2.40)$$

Since every strain component in the out-of-plane direction is zero, according to (2.11), plane strain is enforced. To illustrate the differences between models, the uniaxial deformation problem is considered, where one dimension is stretched by δ , while the other dimensions are kept constant. The deformation tensor is

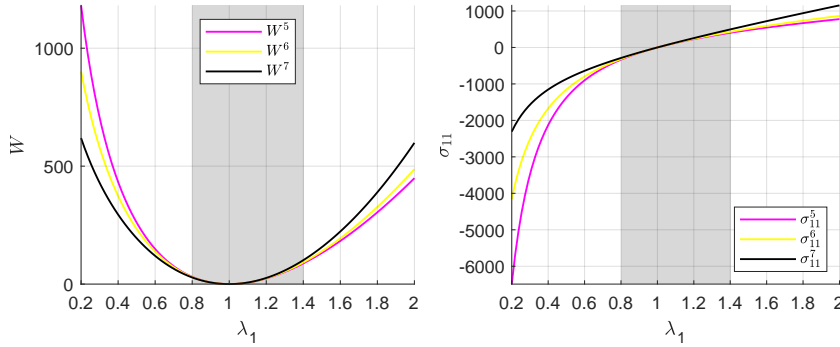
$$\mathbf{C} = \begin{bmatrix} \delta^2 & 0 & 0 \\ 0 & 1 & 0 \\ 0 & 0 & 1 \end{bmatrix} \quad (2.41)$$

which satisfies (2.40). The energy and stress curves are shown in Figure 2.1 where the superscript identifies the model as defined in Table 2.1.



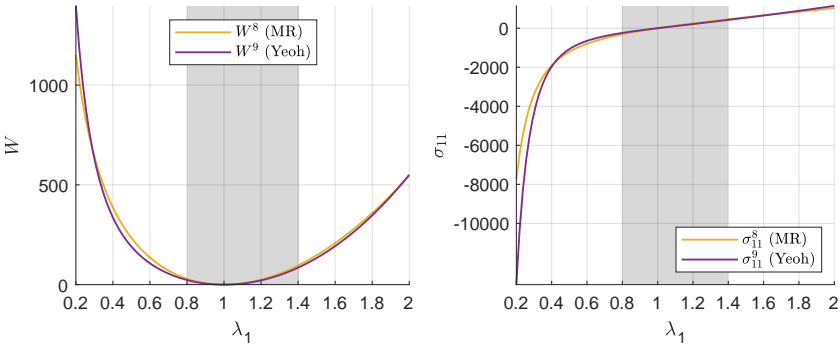
2.1(a): Energy for SVK-based materials.

2.1(b): Stress for SVK-based materials.



2.1(c): Energy for nH-based materials.

2.1(d): Stress for nH-based materials.



2.1(e): Energy for MR and Yeoh.

2.1(f): Stress for MR and Yeoh.

Figure 2.1: Strain energy density and first principal Cauchy stress curves for different models in uniaxial deformation. Similar behavior is observed in the light gray region.

The stretch range in this analysis is $0.2 \leq \lambda_1 \leq 2.0$, with $E = 1000$ and $\nu = 0.3$. From (2.23), (2.24), (2.25) the Lamé's parameters and bulk modulus were computed. The remaining constants were set to the following: $A_{10} = A_{01} = A_{20} = \mu/4$, $A_{30} = D_3 = 0$ and $D_2 = 10^9$. The remaining quantities were calculated from (2.23), (2.24), (2.25) and (2.31).

It is important to observe that the stress in some models (*e.g.*, W^1) does not tend to negative infinity as they are compressed, which may result either in non-realistic behavior or numerical instabilities. This issue is easily addressed in models with one or more compressibility parameters that can be changed independently, to make the material more or less stiff, facilitating convergence.

Lastly, most models perform very similarly within the range $0.8 \leq \lambda_1 \leq 1.4$ (shown as the light gray region in Figure 2.1), so their behavior is very similar in most applications with small enough deformation.

2.3

Finite Element Equations

In static structural analysis, displacement-based nonlinear FEA consists of finding the nodal displacement vector \mathbf{u} of a mesh subject to applied loads and boundary conditions. Most steps of the following derivations will be skipped for conciseness of this text. Hence, for further information on these derivations, the reader is referred to Kim (2014).

For hyperelastic materials, the finite element equations can be derived from the principle of minimum potential energy which states that an elastic system is in equilibrium when its potential energy is minimum. The system's potential energy Π is defined as

$$\Pi(\mathbf{d}) = \Pi^{\text{int}}(\mathbf{d}) - \Pi^{\text{ext}}(\mathbf{d}) \quad (2.42)$$

where $\Pi^{\text{int}}(\mathbf{d})$ is the stored strain energy and $\Pi^{\text{ext}}(\mathbf{d})$ is the work done by external forces. Notice that Π^{int} depends only on the current state of deformation for hyperelastic materials, as defined in Section 2.1.3. The minimum potential energy can be obtained from the perturbation method, which states that the potential Π is at a minimum when its first variation $\delta\Pi$ is zero, that is:

$$\delta\Pi(\mathbf{d}, \bar{\mathbf{d}}) \equiv \left. \frac{d}{d\alpha} \Pi(\mathbf{d} + \alpha\bar{\mathbf{d}}) \right|_{\alpha=0} = 0 \quad \forall \bar{\mathbf{d}} \quad (2.43)$$

where α is the perturbation and $\bar{\mathbf{d}}$ is the variation of the displacement. Substituting (2.43) into (2.42) yields an equation in the form

$$a(\mathbf{d}, \bar{\mathbf{d}}) = l(\bar{\mathbf{d}}) \quad (2.44)$$

where the left-hand side is called the energy form and the right-hand side is the load form. The variational problem is then linearized and discretized into finite elements, whose nodal displacements \mathbf{u} are sought in the deformed configuration. To do so, the problem is posed as finding the increment of nodal displacement $\Delta \mathbf{u}$ that satisfies the following linear system:

$$\mathbf{r} = \mathbf{K}_T \Delta \mathbf{u} \quad (2.45)$$

where \mathbf{K}_T is the tangent stiffness matrix and \mathbf{r} is the residual (or unbalanced force vector) given by

$$\mathbf{r} = \mathbf{f}_{ext} - \mathbf{f}_{int}, \quad (2.46)$$

where \mathbf{f}_{ext} and \mathbf{f}_{int} are the nodal external and internal force vectors, respectively, in the global scope. The applied load is divided in smaller parts, called load steps, where \mathbf{f}_{ext} is assembled proportionally to a given load factor, a procedure known as load control.

The standard NR method is based on iteratively solving the linear system (2.45) until a convergence criterion is satisfied. In this work, the criterion is that the euclidean norm of the residual must be smaller than a given tolerance (10^{-3} unless otherwise stated). At every iteration, \mathbf{f}_{int} and \mathbf{K}_T are computed from the contributions of each element \mathbf{f}_e and \mathbf{K}_e . These quantities are derived for a hyperelastic material at element level (assuming that the external force does not depend on \mathbf{u}) from the following equations:

$$\mathbf{f}_e = \frac{\partial}{\partial \mathbf{u}_e} \int_{\Omega_e^0} W_e dV = \int_{\Omega_e^0} \frac{\partial W_e}{\partial \mathbf{u}_e} dV, \quad (2.47)$$

$$\mathbf{K}_e = \frac{\partial \mathbf{f}_e}{\partial \mathbf{u}_e}. \quad (2.48)$$

where W_e is the element's strain energy in the deformed configuration and Ω_e^0 is the undeformed configuration of element e . Equations (2.47) and (2.48) are particularly useful when deriving the interpolation's expressions in Section 3.2. For implementation purposes, it can be shown that the aforementioned quantities may also be obtained from the following equations:

$$\mathbf{f}_e = \int_{\Omega_e^0} \mathbf{B}_N^T \mathbf{S} dV, \quad (2.49)$$

$$\mathbf{K}_e = \int_{\Omega_e^0} [\mathbf{B}_N^T \mathbf{D} \mathbf{B}_N + \mathbf{B}_G^T \mathbf{\Sigma} \mathbf{B}_G] dV, \quad (2.50)$$

where the quantities in the integrands are evaluated at element-level in the reference configuration of the element; \mathbf{B}_N and \mathbf{B}_G are the nonlinear and linear (geometric) displacement-strain matrix, respectively; \mathbf{S} and \mathbf{D} are computed from (2.20) and (2.21), respectively.

The matrix $\mathbf{\Sigma}$ is defined as

$$\mathbf{\Sigma} = \begin{bmatrix} \mathbf{S} & \mathbf{0} \\ \mathbf{0} & \mathbf{S} \end{bmatrix} \quad (2.51)$$

where $\mathbf{0}$ is a 2×2 null matrix. These integrals were solved using Gaussian integration rule with 2x2 integration points for both the 4- and 8-nodes quadrilateral elements, known as Q4 and Q8, respectively.

The contribution of each element is stored in a global vector (or matrix) through a procedure known as assembly, that is:

$$\mathbf{f}_{int} = \bigcap_{e=1}^{Ne} \mathbf{f}_e, \quad (2.52)$$

$$\mathbf{K}_T = \bigcap_{e=1}^{Ne} \mathbf{K}_e, \quad (2.53)$$

where \bigcap is the assembly operator required to arrange the components into \mathbf{f}_{int} and \mathbf{K}_T . For the linear FEM, the stored strain energy W_e^L of each element can be computed from its linear tangent stiffness matrix \mathbf{K}_e^L by the following quadratic form:

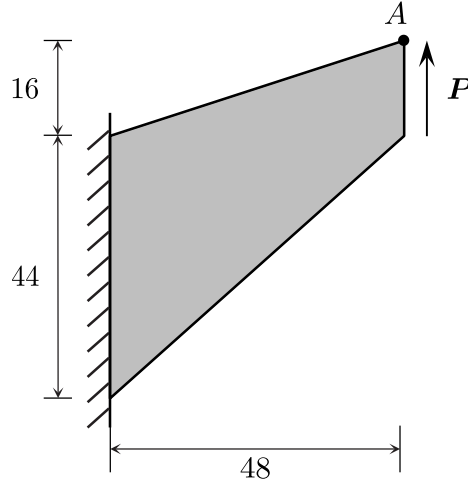
$$W_e^L = \frac{1}{2} \mathbf{u}_e^T \mathbf{K}_e^L \mathbf{u}_e. \quad (2.54)$$

2.3.1

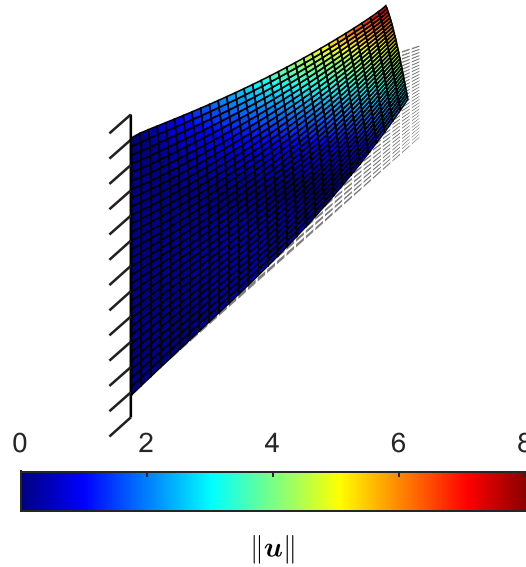
Cook's membrane problem

A benchmark problem is used to verify the FEA code and compare the different nonlinear models: Cook's problem, a "test for combined bending and shear response with moderate distortion" (Dassault, 2010, section 2.1.5). Figure

2.2(a) shows the structure's geometry which is fixed on the left side and a unitary shear force \mathbf{P} is applied on the right edge, whose uppermost node, A , is used as a reference. The external force is vertical at every loading step, *i.e.*, it does not follow nodal rotation. The mesh is composed of 30×30 Q8 plane strain elements with unitary thickness as shown in Figure 2.2(b) in the deformed state .



2.2(a): Problem's domain.



2.2(b): Vertical displacement field using model W^1 (undeformed mesh in light gray).

Figure 2.2: Cook's membrane problem (units in mm).

This problem is often solved for a nearly incompressible neo-Hookean material with $\mu = 0.8$ and $K = 8000$, where the vertical displacement u_y of node A is used as a reference for comparison. The results of this analysis for the SVK and nH models in Table 2.1 are shown in Table 2.2 where the ANSYS' nearly incompressible neo-Hookean model is equivalent to W^8 with $A_{01} = 0$.

Table 2.2: u_y for SVK and nH materials.

Material model W	u_y (mm)
W^1	6.6282
W^2	6.8393
W^3	6.8393
W^4	6.8393
W^5	6.8918
W^6	6.8918
W^7	6.8918
nH (ANSYS)	6.8918

Despite the small differences between each model, the modified nH models were used for comparison with other authors (Simo & Armero, 1992; Brink & Stein, 1996) and have presented excellent agreement with the references, thus validating the analysis. The equilibrium path is shown in Figure 2.3 for the neo-Hookean models from the MATLAB code and using Ansys. Notice that all formulations seem to have similar performances, and further tests have shown that significant differences in displacements and deformation are only observed for very high loads.

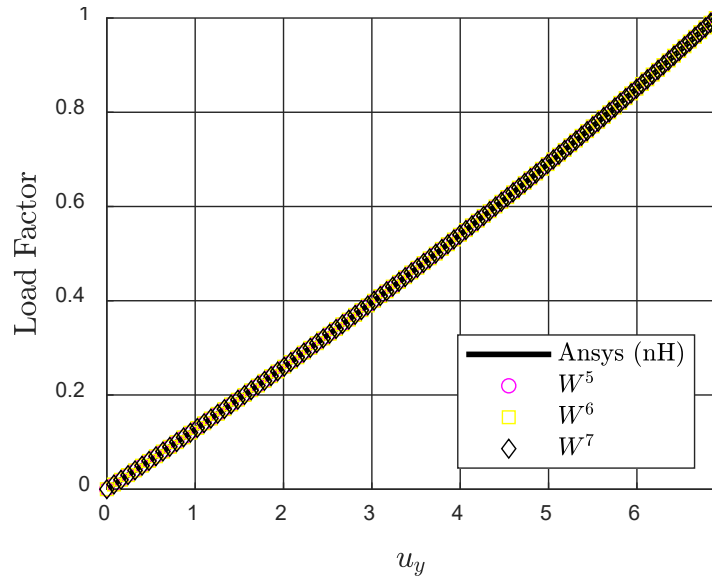


Figure 2.3: Vertical displacement (in millimeters) of the reference node for nH based models.

The same analysis was reproduced for the SVK models in Table 2.1 using similar parameters, with the same adaptations described in Section 2.2.

A slight discrepancy between Ansys and W^1 occurs at higher loadings as shown in the enhanced plot in Figure 2.4. This is because commercial programs like ABAQUS and Ansys define $\boldsymbol{\sigma}$ as a linear function of $\boldsymbol{\varepsilon}$ by default (Kim, 2014, p. 211-212), instead of \mathbf{S} and \mathbf{E} , respectively.

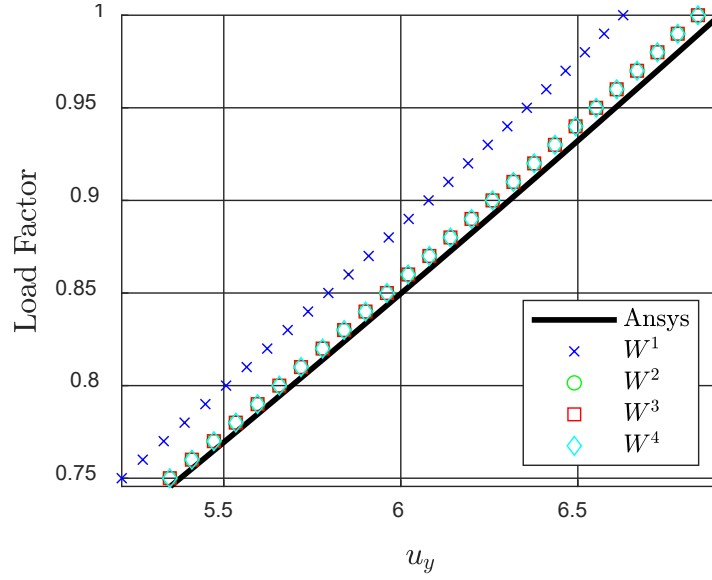


Figure 2.4: Vertical displacement (in millimeters) of the reference node for SVK based materials and Ansys' default model.

The displacement of the reference node for a neo-Hookean material and the equilibrium path depicted in Figure 2.3 agree with the aforementioned references and Ansys, respectively.

3

Topology Optimization

FEM implementation of density-based TO begins with choosing a suitable domain Ω whose mesh properly defines the analyzed structure in bitmap representation. Figure 3.1 illustrates the design domain during an optimization, where $\partial\Omega$ is the domain's boundary, which is divided into Ω_S and Ω_V , the solid and void regions, respectively. Displacement boundary conditions and traction \mathbf{t} are applied to Γ_D and Γ_N , respectively.

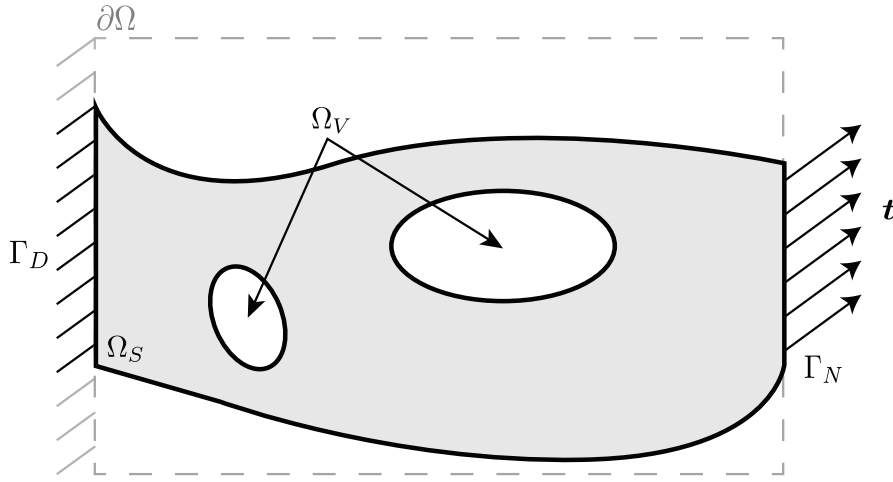


Figure 3.1: Design domain of a TO problem (Leitão & Pereira, 2019, adapted).

To distinguish both regions, a design variable x_e is associated to each element, such that $x_e = 1$ for solid and $x_e = 0$ for void. An optimized domain formed only by “ones and zeros” is sought. However, in order to avoid using discrete valued design variables,

“the most commonly used approach to solve this problem is to replace the integer variables with continuous ones and then introduce some form of penalty that steers the solution to discrete 0-1 values” (Bendsøe & Sigmund, 2002, p. 5, adapted).

Topology optimization can be posed as a minimization problem, essentially, where a vector of design variables \mathbf{x} that minimizes a measure of structural performance is sought. This objective function can be computed from a

FEA, where each element's stiffness is affected by its respective design variable x_e , as described in Section 3.2. The optimization problem is posed as follows:

$$\min_{\mathbf{x}} \quad c = \mathbf{f}_{ext}^T \mathbf{u} \quad (3.1a)$$

$$\text{s.t.} \quad \frac{V(\mathbf{x})}{V_{\Omega}} - V_{frac} \leq 0 \quad (3.1b)$$

$$0 \leq x_e \leq 1 \quad (3.1c)$$

$$\text{with} \quad \mathbf{r}(\mathbf{x}, \mathbf{u}) = \mathbf{f}_{ext} - \mathbf{f}_{int} \approx \mathbf{0}. \quad (3.1d)$$

The objective function in (3.1a) is the end compliance. The constraint in (3.1b) determines that the ratio between the current volume V and the volume of the initial domain V_{Ω} should be less than a fraction V_{frac} . V is computed from each element's contribution by the following expression

$$V(\mathbf{x}) = \sum_{e=1}^{N_e} V_e \bar{x}_e(\mathbf{x}) \quad (3.2)$$

where V_e is the volume of element e and $\bar{x}_e(\mathbf{x})$ is the projected variable defined in Section 3.1.2. Equation (3.1c) establishes the lower and upper bounds of the design variable. Equation (3.1d) states that structural equilibrium is satisfied at every TO iteration (whithin the NR tolerance).

This chapter is divided in three parts:

Section 3.1 briefly introduces the optimization method, filter, projection and penalization used;

Section 3.2 presents the interpolation methods used in this thesis and compares their performance analyzing the deformation of a C-shaped structure;

Section 3.3 closes the chapter by deducing the sensitivity equations that are validated with a numerical example.

3.1

Optimization algorithm

Many optimization algorithms have been proposed in the literature and seek to minimize a given objective function in a sequence of guesses for the optimal vector of design variables \mathbf{x} . This procedure may or may not require further information from the objective function, namely its derivatives with respect to the design variables, called the sensitivities.

A well-spread algorithm known as Optimality Criteria (OC) has been widely used in linear topology optimization since it considers a single constraint, usually the structure's volume or weight. However, the standard OC method found in the literature (Talischi *et al.*, 2012) presents a notable drawback: for usual parameters, the square root of the sensitivity is needed. While in linear analysis it may be shown that sensitivity is always non-negative (Bendsoe & Sigmund, 2002), the same is not true in nonlinear analysis and may hinder the optimization process.

The Method of Moving Asymptotes (MMA) proposed by Svanberg (1987) is often used for structural optimization with more than one constraint or nonlinearities in general. It works by minimizing an extended objective function that can be written as the following minimization problem:

$$\min_{\mathbf{x}} \quad f_0(\mathbf{x}) + a_0 z + \sum_{i=1}^m \left(c_i y_i + \frac{1}{2} d_i y_i^2 \right) \quad (3.3a)$$

$$\text{s.t.} \quad f_i - a_i z - y_i \leq 0 \quad i = 1, \dots, m \quad (3.3b)$$

where \mathbf{y} and z are artificial optimization variables and a_0 , c_i and d_i are constants to be adjusted according to the problem. In order to apply the MMA to the minimum compliance problem, f_0 is the end-compliance in (3.1a) and f_i is a single volume constraint in (3.1b).

The reader is referred to the original article for information on this method's derivation (Svanberg, 1987). Details on a MATLAB implementation were provided by Svanberg (2007) along with a proper choice of the constants in the standard optimization problem (with $i = 1$ constraint): $a_0 = d_1 = 1$, $a_1 = 0$ and c_1 is a large number. This set of parameters ensures that the artificial variables go to zero, yielding the optimal values for \mathbf{x} as desired. The choice of c_1 has shown to largely influence the results and has been set to 10^7 unless otherwise stated.

The optimization algorithm uses the value of the objective function and its derivatives to find a new set of design variables at every iteration. In

practice, however, an element's stiffness is penalized by its respective density \hat{x} , which is indirectly calculated from the design variable through a sequence of techniques shown in Figure 3.2 .

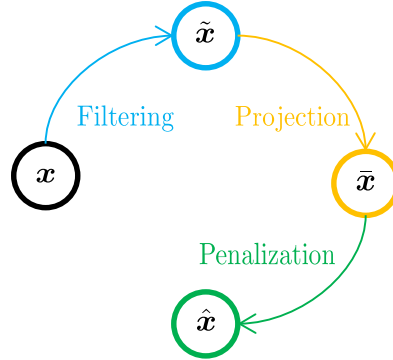


Figure 3.2: Design variable, filtered, projected and penalized.

3.1.1

Filtering

Filters are often implemented in TO algorithms to avoid mesh dependency problems, as depicted in Figure 3.3. Notice that the end optimized topology changes noticeably instead of simply getting more well-defined as the mesh is refined.



3.3(a): 2700 elements.



3.3(b): 4800 elements.



3.3(c): 17200 elements.

Figure 3.3: Variation of optimal result as a function of refinement of the mesh for the MBB beam (Bendsøe & Sigmund, 2002, adapted).

Many solutions were proposed to circumvent this problem including the linear filter of the design variables used by Bruns & Tortorelli (2001). This solution is adopted in this work, as it provides a smoother gradient of the density variable field. Mathematically, this filter is essentially a weighted average of the design variables given by

$$\tilde{x}_e = \frac{\sum_{i=1}^{N_e} w_{e,i} x_i}{\sum_{i=1}^{N_e} w_{e,i}} \quad (3.4)$$

where $w_{e,i}$ is the weight of the average defined as

$$w_{e,i} = \max \left(1 - \frac{d_{e,i}}{r_{min}}, 0 \right) \quad (3.5)$$

where $d_{e,i}$ is the Euclidian distance between the centroids of elements e and i , and r_{min} is the radius of the filter. Implementation-wise, the filter is applied in matrix form, that is,

$$\tilde{\mathbf{x}} = \mathbf{M} \mathbf{x} \quad (3.6)$$

where elements of \mathbf{M} are defined directly from (3.4) as

$$M_{e,i} = \frac{w_{e,i}}{\sum_{i=1}^{N_e} w_{e,i}}. \quad (3.7)$$

Figure 3.4 shows a illustration of the top and front views of the filter in a regular mesh.

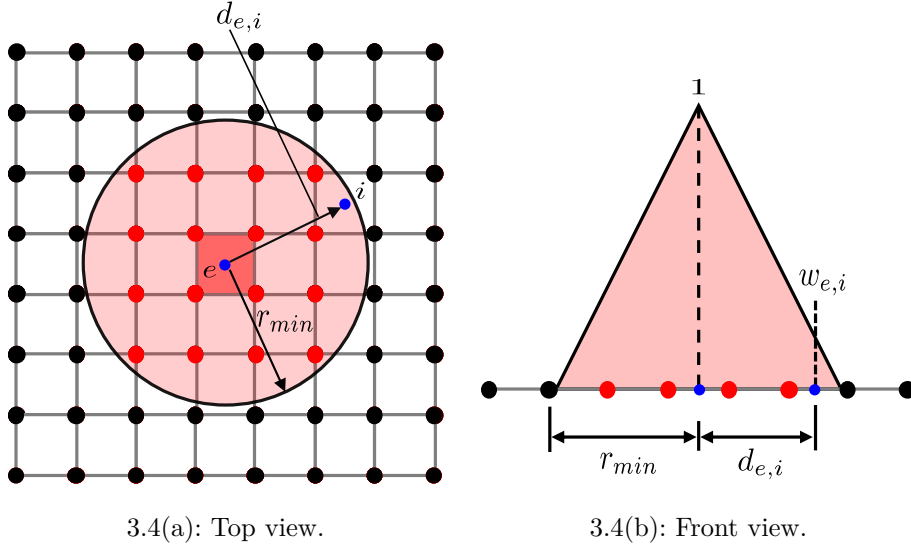


Figure 3.4: Linear filter (Leitão & Pereira, 2019, adapted).

3.1.2 Projection and Penalization

A Heaviside projection can be utilized to remove gray tones (values that are not close to the limits 0 and 1) in the final topology. However, in order to provide a steep transition, without the loss of continuity, a smoothed Heaviside projection introduced by Wang *et al.* (2011) is used as follows

$$\bar{x}_e(\tilde{x}_e) = \frac{\tanh(\beta\eta) + \tanh[\beta(\tilde{x}_e - \eta)]}{\tanh(\beta\eta) + \tanh[\beta(1 - \eta)]}. \quad (3.8)$$

where β and η are the sharpness parameter and the threshold variable, respectively. The effects of the smoothed Heaviside projection are shown in Figure 3.5, where it's clear that the transition from zero to one gets progressively steeper with the increase of β . The values $\beta = 4$ and $\eta = 0.5$ are used in this work unless otherwise stated.

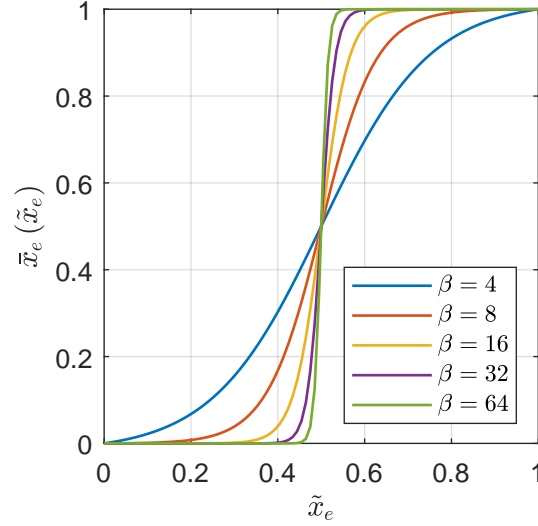


Figure 3.5: Smoothed Heaviside projection ($\eta = 0.5$) for different values of β .

The penalization is “used to ensure black-and-white designs in density-based topology optimization (typically $p = 3$)” (Wang *et al.*, 2014, adapted). The SIMP method introduced by Bendsøe (1989) is used, where the design variable is raised to a power $p > 1$ subject to continuation. The element density is calculated from

$$\hat{x}_e(\bar{x}_e) = (1 - \epsilon)\bar{x}_e^p + \epsilon \quad (3.9)$$

where p is the penalization factor and ϵ , the so-called Ersatz parameter, is set to 10^{-9} unless otherwise stated, and helps avoiding numerical instabilities during the solution of the linear systems in FEA. Figure 3.6 shows the effect of the SIMP method for common values of the penalization parameter, where it can be seen that the curve get steeper as p increases.

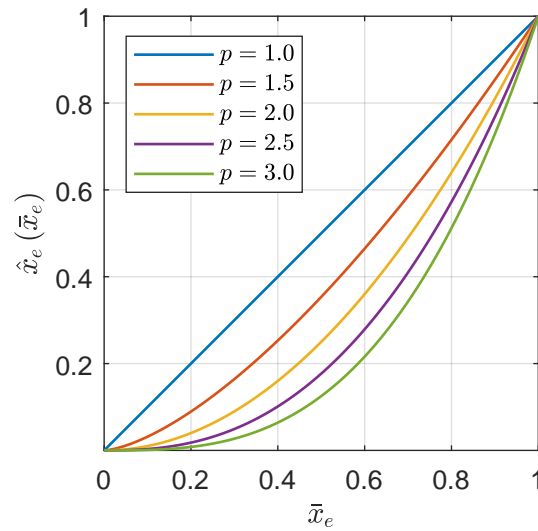


Figure 3.6: Penalization of the projected variable for different values of p .

3.2

Interpolation methods

During the TO process, the mesh is composed of elements whose behavior depends on its strain energy. Two methods presented in the literature proposed interpolating the strain energy density W_e of each element as a function of its density, such that low-density elements are formulated utilizing a less stiff model. To better illustrate this concept, consider the C-shaped structure depicted in Figure 3.7.

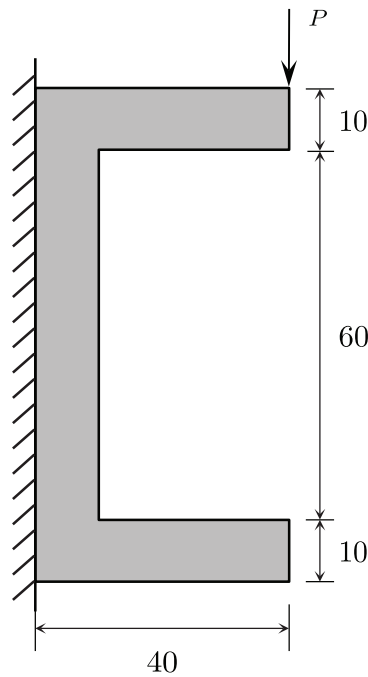
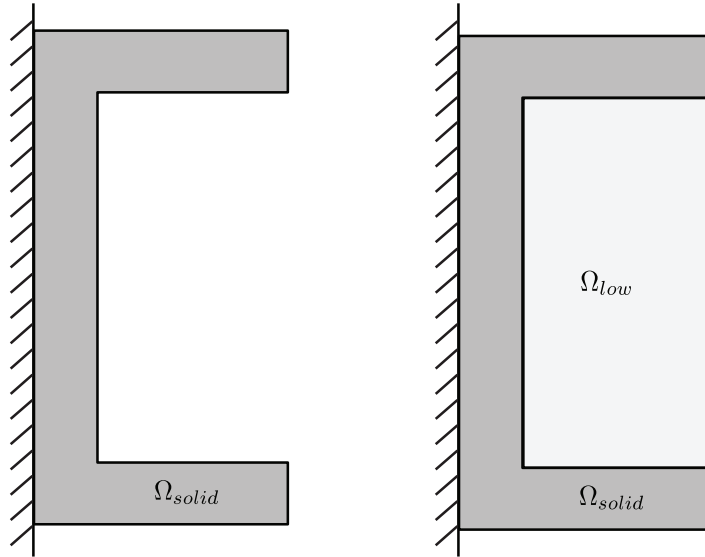


Figure 3.7: C-shape problem domain (units in mm) (Luo *et al.*, 2015, adapted).

A regular mesh of Q4 elements properly describes the structure to be analyzed, however, during a TO process, a rectangular domain may have been chosen, such that the same structure would have to be represented with both solid and low-density elements. Figure 3.8 shows the two domains that represent the problem's geometry, where $x_e = 1$ for elements in the solid region Ω_{solid} and $x_e = x_{low} > 0$ for elements in the void region Ω_{low} . The mesh is omitted for legibility.



3.8(a): Domain without low-density elements (1400 elements in the mesh).

3.8(b): Domain with low-density elements (3200 elements in the mesh).

Figure 3.8: C-shape domain using Q4 elements (dark gray: solid elements; light gray: low-density elements).

Although performing a FEA on a mesh composed only by solid elements is more desirable, every element in the domain should be considered in the calculations (unless an element removal technique is used, such as those presented in Section 1.2). Table 3.1 presents the interpolation methods for low-density elements considered in this work, which aim to help the FEA converge in more difficult cases.

In the following subsections, the superscripts L and NL are used to refer to linear and nonlinear models, respectively. Thus, implementation-wise, NL is a number that represents a hyperelastic material model as defined in Table 2.1). Some alterations have been made to the original methods (*e.g.*, penalization, convergence criteria and update schemes) to compare them on even ground.

Table 3.1: Model of the void region for each interpolation methods.

Author	Method	Void Region Model
Wang <i>et al.</i> (2014)	Energy Interpolation	Linear (W^L)
Luo <i>et al.</i> (2015) Chen <i>et al.</i> (2019a)	Additive Hyperelasticity	Yeoh

3.2.1

No interpolation (None)

Early works in GNL TO such as Buhl *et al.* (2000) and Pedersen *et al.* (2001) proposed a penalization of the constitutive tensor in order to change each element stiffness, without any interpolation method. This penalization does not work for hyperelastic materials that may not have a linear stress-strain relationship, since the stress \mathbf{S} in (2.50) (assembled in matrix $\mathbf{\Sigma}$) is not necessarily computed from the constitutive tensor. In this sense, penalizing only the constitutive tensor would not affect both terms that compose the tangent stiffness matrix in a GNL analysis.

A more general approach similar to that used by Klarbring & Strömberg (2013), is reproduced here by penalizing the element's strain energy instead, that is,

$$W_e(\hat{x}_e, \mathbf{u}_e) = \hat{x}_e W_e^{NL}(\mathbf{u}_e) \quad (3.10)$$

Notice that the same equation is used to penalize every element's stiffness, so both solid and void elements are modeled after the same nonlinear formulation. The element's internal force vector and tangent stiffness matrix can be calculated from its strain energy. Substituting (3.10) into (2.47) yields

$$\mathbf{f}_e(\hat{x}_e, \mathbf{u}_e) = \hat{x}_e \mathbf{f}_e^{NL}(\mathbf{u}_e), \quad (3.11)$$

Likewise, substituting (3.11) into (2.48) yields

$$\mathbf{K}_e(\hat{x}_e, \mathbf{u}_e) = \hat{x}_e \mathbf{K}_e^{NL}(\mathbf{u}_e). \quad (3.12)$$

3.2.2

Energy Interpolation (EI)

This technique proposed by Wang *et al.* (2014) is based on interpolating the strain energy density of an element between a nonlinear and linear model given by

$$W_e(\hat{x}_e, \gamma_e, \mathbf{u}_e) = [W_e^{NL}(\gamma_e \mathbf{u}_e) - W_e^L(\gamma_e \mathbf{u}_e) + W_e^L(\mathbf{u}_e)] \hat{x}_e \quad (3.13)$$

where γ_e is the element's interpolation factor. For the purposes of this work, the strain energy density of the element is penalized (instead of the Young modulus, as in the original work) in order to enable the use of different material models defined in terms of its strain energy (instead of just E and ν). Substituting (2.54) in (3.13), after a few manipulations, yields

$$W_e(\hat{x}_e, \gamma_e(\bar{x}_e), \mathbf{u}_e) = [W_e^{NL}(\gamma_e \mathbf{u}_e) + (1 - \gamma_e^2)W_e^L(\mathbf{u}_e)] \hat{x}_e. \quad (3.14)$$

Notice that, due to the nonlinearity of W_e^{NL} , γ_e cannot be explicitly written as done for the W_e^L . A smoothed Heaviside projection is used to calculate the interpolation factor as a function of the projected variable \bar{x}_e as follows:

$$\gamma_e(\bar{x}_e) = \frac{\tanh(\beta_1 \rho_0) + \tanh[\beta_1(\bar{x}_e^p - \rho_0)]}{\tanh(\beta_1 \rho_0) + \tanh[\beta_1(1 - \rho_0)]}. \quad (3.15)$$

This projection provides a continuous yet swift transition between linear to nonlinear formulation as \bar{x}_e increases, where p is the penalization factor described in Section 3.1.2. The sharpness parameter β_1 affects the transition slope whose midpoint is determined by the threshold variable ρ_0 .

Despite the similarities between (3.8) and (3.15), these projections are used in different contexts and should not be confused. For the purposes of this text, unless otherwise stated, it has been chosen $\beta_1 = 500$ and $\rho_0 = 0.01$, the same as Wang *et al.* (2014), which provide a steep transition close to $\bar{x}_e = 0.01$ for $p = 1$, as shown in Figure 3.9.

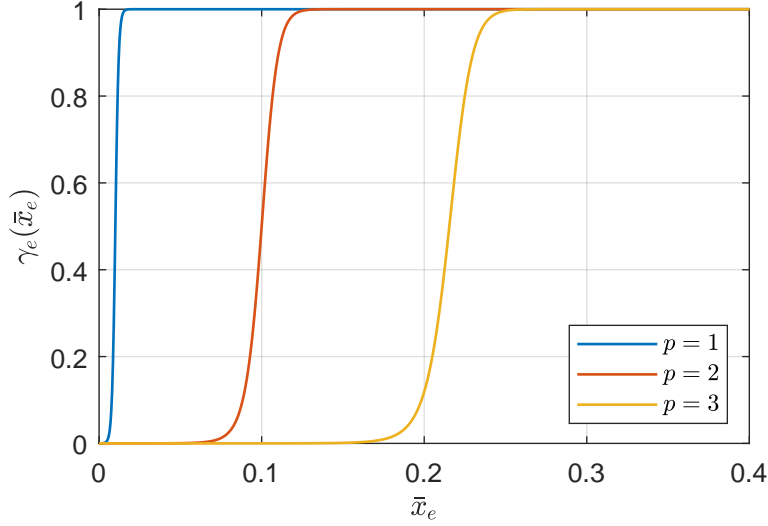


Figure 3.9: Interpolation parameter's projection for different values of p .

The element's internal force is obtained for this interpolation technique by substituting (3.14) into (2.47), which yields

$$\begin{aligned}
 \mathbf{f}_e(\hat{\mathbf{x}}_e, \gamma_e, \mathbf{u}) &= \int_{\Omega_e^0} \frac{\partial}{\partial \mathbf{u}} \left\{ \left[W_e^{NL}(\gamma_e \mathbf{u}_e) + (1 - \gamma_e^2) W_e^L(\mathbf{u}_e) \right] \hat{\mathbf{x}}_e \right\} dV \\
 &= \left[\int_{\Omega_e^0} \frac{\partial W_e^{NL}(\gamma_e \mathbf{u}_e)}{\partial(\gamma_e \mathbf{u})} \frac{\partial(\gamma_e \mathbf{u})}{\partial \mathbf{u}} dV + (1 - \gamma_e^2) \int_{\Omega_e^0} \frac{\partial W_e^L(\mathbf{u}_e)}{\partial \mathbf{u}} dV \right] \hat{\mathbf{x}}_e \\
 &= \left[\gamma_e \mathbf{f}_e^{NL}(\gamma_e \mathbf{u}_e) + (1 - \gamma_e^2) \mathbf{f}_e^L(\mathbf{u}_e) \right] \hat{\mathbf{x}}_e \quad (3.16)
 \end{aligned}$$

where L and NL subscripts refer to the linear and nonlinear force vectors. Likewise for the tangent stiffness matrix, substituting (3.16) into (2.48) yields

$$\begin{aligned}
 \mathbf{K}_e(\hat{\mathbf{x}}_e, \gamma_e, \mathbf{u}) &= \frac{\partial}{\partial \mathbf{u}} \left[\gamma_e \mathbf{f}_e^{NL}(\gamma_e \mathbf{u}_e) + (1 - \gamma_e^2) \mathbf{f}_e^L(\mathbf{u}_e) \right] \hat{\mathbf{x}}_e \\
 &= \left[\gamma_e \frac{\partial \mathbf{f}_e^{NL}(\gamma_e \mathbf{u}_e)}{\partial(\gamma_e \mathbf{u})} \frac{\partial(\gamma_e \mathbf{u})}{\partial \mathbf{u}} + (1 - \gamma_e^2) \frac{\partial \mathbf{f}_e^L(\mathbf{u}_e)}{\partial \mathbf{u}} \right] \hat{\mathbf{x}}_e \\
 &= \left[\gamma_e^2 \mathbf{K}_e^{NL}(\gamma_e \mathbf{u}_e) + (1 - \gamma_e^2) \mathbf{K}_e^L(\mathbf{u}_e) \right] \hat{\mathbf{x}}_e. \quad (3.17)
 \end{aligned}$$

3.2.3

Additive Hyperelasticity (AH)

The last technique presented in this section was idealized by Luo *et al.* (2015) and is based on interpolating (or adding) the strain energy density of a “soft” hyperelastic model to each element in a mesh. In this method, the parameters

of an added hyperelastic material can be adjusted during the TO procedure in order to help NR convergence in TO iteration where elements' deformation is excessive.

The original author proposed an explicit interpolation between SVK and a soft incompressible Yeoh material for the void regions. Chen *et al.* (2019a) implemented this technique using ANSYS to perform the FEA, which led to two important changes: first, the use of a nearly incompressible nH material instead of SVK due to its better performance under compression; second, the use of nearly incompressible Yeoh model for the additive material.

Table 3.2: Models used with the AH interpolation by different authors.

Author	Assumption	Base model	Additive Yeoh model
Luo <i>et al.</i> (2015)	Plane stress	SVK	Incompressible
Chen <i>et al.</i> (2019a)		nH	Nearly incomp.
This work	Plane strain	Varies	Nearly incomp.

Table 3.2 shows important details on the different iterations of the AH method throughout these works, where it is important to notice that this work implements it to plane strain problems, whereas the first works have implemented it to analyses in plane stress. The strain energy density for the AH is given by the following interpolation

$$W_e(\hat{x}_e, \mathbf{u}) = \hat{x}_e W_e^{NL} + (1 - \hat{x}_e) W_e^Y \quad (3.18)$$

where W_e^Y is a the strain energy density of the added Yeoh material, as described in Table 3.1. The parameters A_{10} , A_{20} , A_{30} , D_1 and D_2 of the added material are the same for all elements e during the FEA. Figure 3.10 illustrates the remodeled element after the interpolation, which behaves exactly as if an element with the hyperelastic material $(1 - \hat{x}_e) W_e^Y$ was added “on top of” the original one.

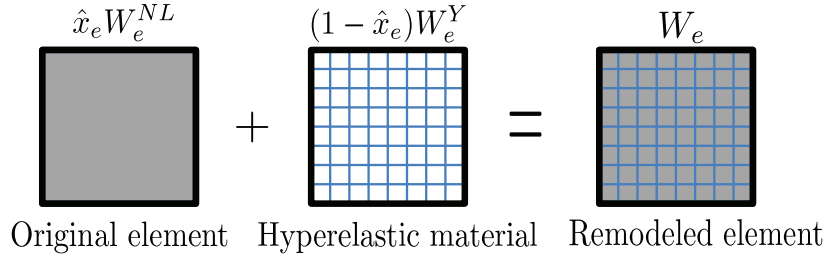


Figure 3.10: Schematic representation of the AH method (Luo *et al.*, 2015, adapted)

The internal force vector of an element is obtained following the same steps as in Section 3.2.1, but considering the term W_e^Y :

$$\mathbf{f}_e(\hat{x}_e, \mathbf{u}_e) = \hat{x}_e \mathbf{f}_e^{NL}(\mathbf{u}_e) + (1 - \hat{x}_e) \mathbf{f}_e^Y(\mathbf{u}_e) \quad (3.19)$$

where \mathbf{f}_e^Y is the force vector computed from the added Yeoh material. Likewise, the element's tangent stiffness matrix is obtained from the nonlinear part \mathbf{K}_e^{NL} and the one from the Yeoh model \mathbf{K}_Y . Substituting (3.19) into (2.48) yields

$$\mathbf{K}_e(\hat{x}_e, \mathbf{u}_e) = \hat{x}_e \mathbf{K}_e^{NL}(\mathbf{u}_e) + (1 - \hat{x}_e) \mathbf{K}_e^Y(\mathbf{u}_e). \quad (3.20)$$

The nearly incompressible Yeoh model was used in this work, rather than the incompressible Yeoh model, due to difficulties intrinsic to plane strain problems. Commercial programs such as ABAQUS address this limitation in its documentation:

“Except for plane stress and uniaxial cases, it is not possible to assume that the material is fully incompressible in ABAQUS/-Explicit because the program has no mechanism for imposing such a constraint at each material calculation point. Instead, we must provide some compressibility.” (Dassault, 2007, section 17.5.1)

3.2.3.1

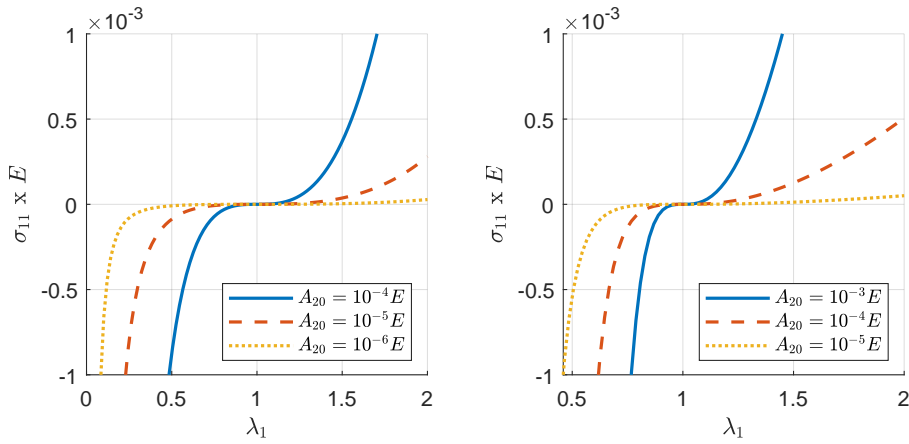
Additive Hyperelasticity parameters

The proper choice of parameters A_{m0} and D_i are paramount to the AH interpolation method. While the former influences the distortional aspect of the low-density elements, the latter affects their compressibility. The choice of the model's parameters for this work are explained in greater detail in the following paragraphs.

- Hyperelastic parameters A_{10} , A_{20} and A_{30} :

The original article (Luo *et al.*, 2015) investigated the effects of constants A_{m0} on the model's performance. A_{10} was set to a small enough value (*i.e.*, $A_{10} = 10^{-9}E$) to make the material sufficiently soft while constants A_{20} and A_{30} were analyzed which concluded that both have similar effects. Thus, A_{30} was set to zero (as it is in this work) and an update scheme for A_{20} was proposed.

A useful range for A_{20} between $10^{-6}E$ and $10^{-4}E$ was determined from analytical results in simple tension (Luo *et al.*, 2015, p. 428), using an incompressible Yeoh model and is reproduced in Figure 3.11(a).



3.11(a): Simple tension assuming incompressibility in plane stress.

3.11(b): Near incompressibility (W^9) assuming plane strain ($D_1 = 2/K$ and $D_2 = 10^9$).

Figure 3.11: Stress-stretch curves for Yeoh models with different values of A_{20} and compressibility formulations.

A similar analysis is shown in Figure 3.11(b) for the nearly incompressible model W^9 : an element is subject to principal stretches $\lambda_1 = \lambda$, $\lambda_2 = \lambda^{-1}$ and $\lambda_3 = 1$ (ensuring plane strain and incompressibility, since $\lambda_3 = 1$ and $J = 1$). The first principal Cauchy stress as a function of λ_1 is shown in Figure 3.11 for both formulations and different values of A_{20} .

It may be observed that a useful range of parameters depends on the formulation considered, so it is expected that A_{20} should range between $10^{-5}E$ and $10^{-3}E$ for plane strain applications.

- Compressibility parameters D_1 , and D_2 :

First, it is recalled that W^9 is a Yeoh model with nearly incompressible formulation, where the compressibility parameters $D_1 = 2/K$ is a

measure of how compressible the material is. In order to simplify this analysis, D_2 is set to a high value such that its respective term vanishes (see W^9 in Table 2.1 for $N = 2$).

It follows that the incompressible behavior may be approximated by using a low enough compressibility parameter D_1 . However, it has been noticed that if both of these compressibility constants are too high (thus, making the added material more compressible), *e.g.*, $D_1 = D_2 = 10^6$, the FEA may not converge (Chen *et al.*, 2019a, p. 1866 and 1877)¹.

The parameters used for the additive material, unless otherwise stated, are presented in Table 3.3 alongside those used by the original authors.

Table 3.3: Parameters of the additive Yeoh material by different authors.

Author	A_{10}	A_{20}	D_1	D_2
Luo <i>et al.</i> (2015)	$(10^{-3})^p E/6$	Variable	-	-
Chen <i>et al.</i> (2019a)	$10^{-9} E$		10^{-9}	10^6
This work	$10^{-9} E/6$	$10^{-9} E$	10^9	10^9

A constant set of parameters were chosen to simplify the implementation while retaining the low stiffness of the added material. The following example illustrates the influence of A_{20} and D_1 in an analysis with significant compression of the void region.

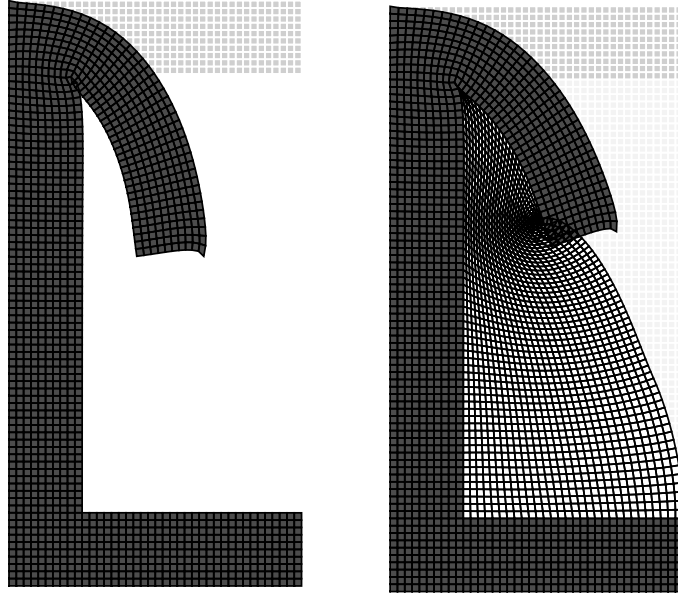
3.2.3.2

C-shape example

The C-shape problem depicted in Figure 3.7 is solved with and without the void region using the AH method. The model used in this analysis is W^2 with $E = 1$ Pa, $\nu = 0.4$ and the load is $P = 0.4$ N. The element's density was set to $\hat{x}_e = 1$ and $\hat{x}_e = 10^{-9}$ for solid and low-density elements, respectively, and unitary thickness is assumed.

The analysis was performed with a constant load step of 5% of the total and a maximum of 20 NR iterations per step. The deformed structure is shown for each case in Figure 3.12 in two scenarios: without the void region and no interpolation (Figure 3.12(a)); with the void region for high compressibility parameter $D_1 = 10^9 \times 2/K$ (Figure 3.12(b)) and $A_{20} = 10^{-3} \times E$.

¹The authors in that work chose not to penalize the compressibility constants in order to preserve convergence properties during the FEA. Since this workaround could introduce a small error to the sensitivity analysis, all parameters are penalized in this work, in agreement with (3.18).



3.12(a): Original mesh
(without void region).

3.12(b): Mesh with void re-
gion with high compress-
ibility.

Figure 3.12: Deformed mesh for the C-shape problem. Undeformed mesh in lighter shades of gray.

It is noted that the analysis did not converge for D_1 smaller than 10^{-6} even for the first load step, since the nearly compressible additive material has no room to deform in plane strain condition. This observation explains the choice of high values for both D_1 and D_2 shown in Table 3.3, but further investigation on the influence of these parameters may enhance the performance of the AH method.

The C-shape problem was reproduced with different values of A_{20} (Figure 3.13), where it can be seen that the analysis tends to converge for higher applied loads as A_{20} increases. The compliance vs load curve is used to justify the choice of the range for A_{20} in this work: a higher value in the order of $10^{-3}E$ makes convergence easier at the cost of a more stiff structural response, while a smaller value in the order of $10^{-5}E$ yields a minor error but converges for smaller loads. Thus, a value $A_{20} = 10^{-9}E$ was chosen to further minimize the error.

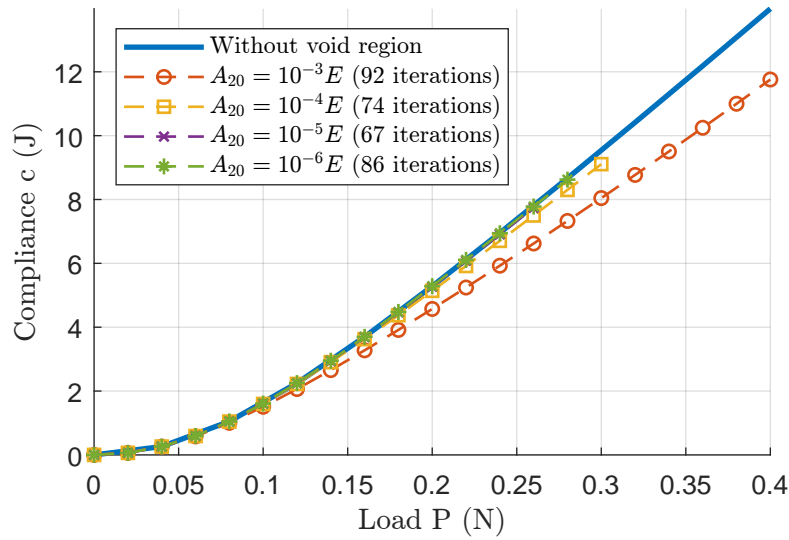


Figure 3.13: Compliance of the C-shape for different values of A_{20} (total NR iterations indicated).

3.2.4

Comparison of the interpolation methods

In order to better compare the differences in the void region's behavior of each interpolation, a second C-shape problem proposed by Yoon & Kim (2005) as shown Figure 3.14 is analyzed, where the same set of parameters used in the previous analysis in Section 3.2.3.2 is considered, except for $\nu = 0.3$ and the applied loads, which are $f_1 = 0.018$ N and $f_2 = 0.027$ N.

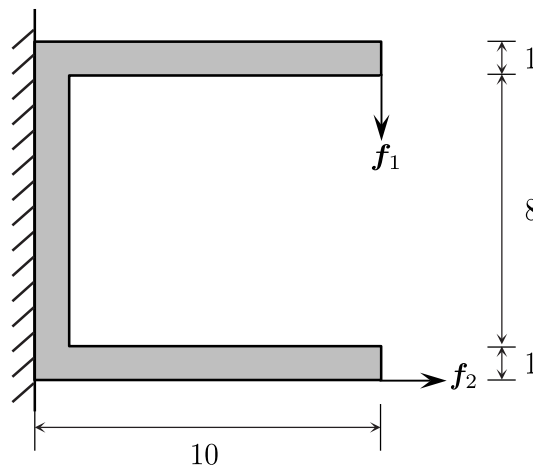
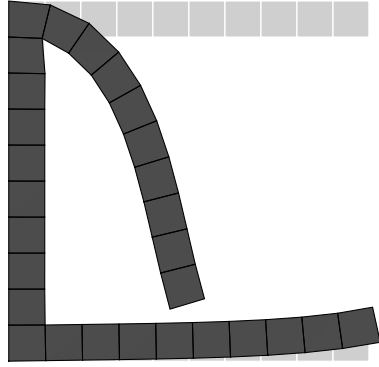


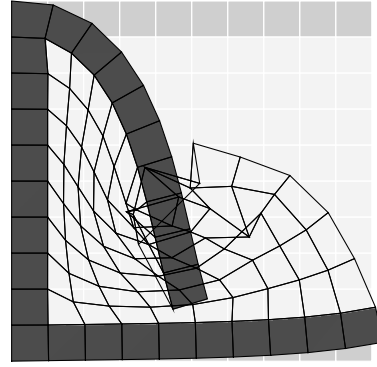
Figure 3.14: Second C-shape problem domain adapted from Wang *et al.* (2014) (units in m).

The mesh is composed by 100 and 28 Q4 elements for the cases with and without the void region, respectively, and the analysis was run with a constant load step size of 5% of the total. Figure 3.15 shows the behavior of

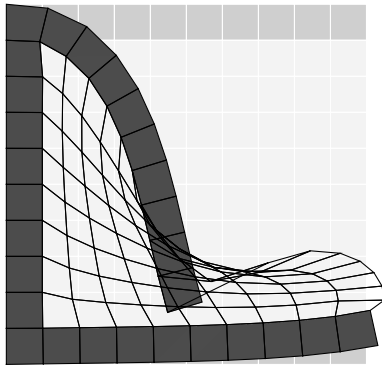
the void region under significant compression, that is noticeably higher than the previous case shown in Figure 3.12.



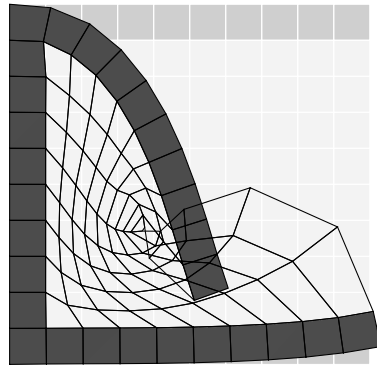
3.15(a): Original mesh (without void region).



3.15(b): No interpolation.



3.15(c): Energy Interpolation.



3.15(d): Additive Hyperelasticity ($A_{20} = 2.5 \times 10^{-5} E$).

Figure 3.15: Deformed mesh for the second C-shape problem. Undeformed mesh in lighter shades of gray.

Figure 3.15(b) presents a distorted void region due to the GNL formulation adopted, whereas 3.15(c) shows a smooth deformed mesh. Wang *et al.* (2014) observed that this is due to the FEA not considering the inversion of the low-density elements, since the stiffness matrices are calculated in the undeformed geometry for linear elements. This is not the case for elements modeled after W_e^Y , thus 3.15(d) presents a more distorted response. However, the total iterations required to converge are significantly reduced using AH compared to not using any interpolation, as shown in Table 3.4.

Table 3.4: Results of the second C-shape problem using a step size of .05

Interpolation method	Iterations	Compliance $\times 10^{-1} N \cdot m$
(a) Without void region	80	1.445585
(b) None	157	1.445585
(c) Energy Interpolation	82	1.445585
(d) Additive Hyperelasticity	85	1.384415

The same problem was solved with a unitary step size and the results are listed in Table 3.5. The EI method was the only one able to converge with a unitary step size, and performed the best in both cases (other than the case without the void region).

Table 3.5: Results of the second C-shape problem using a step size of 1.0

Method	Iterations	Compliance $\times 10^{-1} N \cdot m$
(a) Without void region	12	1.445585
(b) None	Did not converge in 200 iterations	
(c) Energy Interpolation	12	1.445585
(d) Additional Hyperelasticity	Did not converge in 200 iterations	

The problem was solved for a standard value $D_1 = 2/K$ as shown in Figure 3.16 where it is seen that the behavior of nearly incompressible low-density elements under plane strain condition is significantly affected by D_1 , as discussed in Section 3.2.3.1.

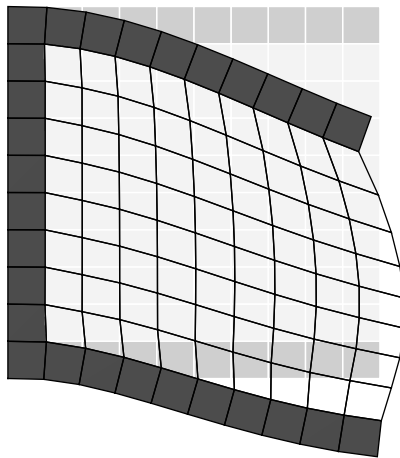


Figure 3.16: Deformed mesh for the second C-shape problem using AH with $D_1 = 2/K$. Undeformed mesh in lighter shades of gray.

3.3

Sensitivity Analysis

The sensitivity is the derivative of a function with respect to the design variables. The sensitivity of the volume constraint is trivial and will not be reproduced in this text, so the reader is referred to Talischi *et al.* (2012), where its derivation is found. The sensitivity of the objective function (3.1a) is derived at element level (for the most part) using the following chain rule:

$$\frac{\partial c(\mathbf{u}, \mathbf{z})}{\partial x_e} = \frac{\partial \tilde{x}_e}{\partial x_e} \frac{\partial \bar{x}_e}{\partial \tilde{x}_e} \frac{\partial \hat{x}_e}{\partial \bar{x}_e} \frac{\partial c}{\partial \hat{x}_e}. \quad (3.21)$$

Starting from the first term on the right-hand side, the derivative of the filtered variables with respect to the design variables can be conveniently obtained in matrix form. Deriving (3.6) with respect to the vector of design variables yields

$$\frac{\partial \tilde{\mathbf{x}}}{\partial \mathbf{x}} = \frac{\partial}{\partial \mathbf{x}} (\mathbf{M}\mathbf{x}) = \mathbf{M}^T. \quad (3.22)$$

Since the filter is linear, its derivative is the transpose of the filtering matrix. The second term on the right-hand side in (3.21) is obtained by deriving (3.8) with respect to \tilde{x}_e as follows

$$\frac{\partial \bar{x}_e}{\partial \tilde{x}_e} = \frac{\beta \operatorname{sech}^2[\beta(\tilde{x}_e - \eta)]}{\tanh(\beta\eta) + \tanh[\beta(1 - \eta)]} \quad (3.23)$$

The third term comes from the SIMP technique and is obtained by deriving (3.9) with respect to \bar{x}_e as follows:

$$\frac{\partial \hat{x}_e}{\partial \bar{x}_e} = p(1 - \epsilon)\bar{x}_e^{p-1}. \quad (3.24)$$

To find the last term in (3.21), it is useful to rewrite the end compliance as a function of the vector of element densities $\hat{\mathbf{x}}$, that implicitly depends on \mathbf{x} . An adjoint vector $\boldsymbol{\lambda}$ is added to (3.1a), which gives

$$c(\mathbf{u}, \hat{\mathbf{x}}) = \mathbf{f}_{ext}^T \mathbf{u} + \boldsymbol{\lambda}^T \mathbf{r}(\mathbf{u}, \hat{\mathbf{x}}) \quad (3.25)$$

where the last term on the right-hand side does not affect the expression, since $\mathbf{f}_{int} = \mathbf{f}_{ext}$ so $\mathbf{r} = \mathbf{0}$ at equilibrium (see (2.46)). Deriving (3.25) at element

level yields

$$\begin{aligned} \frac{\partial c(\mathbf{u}, \hat{\mathbf{x}})}{\partial \hat{x}_e} &= \left(\frac{\partial \mathbf{f}_{ext}}{\partial \hat{x}_e} \right)^T \mathbf{u} + \mathbf{f}_{ext}^T \frac{\partial \mathbf{u}}{\partial \hat{x}_e} \\ &\quad + \boldsymbol{\lambda}^T \left(\frac{\partial \mathbf{r}}{\partial \hat{x}_e} \Big|_{\mathbf{u}=const} + \frac{\partial \mathbf{r}}{\partial \mathbf{u}} \Big|_{\hat{x}_e=const} \frac{\partial \mathbf{u}}{\partial \hat{x}_e} \right) + \frac{\partial \boldsymbol{\lambda}^T}{\partial \hat{x}_e} \mathbf{r} \end{aligned} \quad (3.26)$$

where the first term on the right-hand side was canceled because \mathbf{f}_{ext} does not depend on \hat{x}_e . Moreso, the last term is also neglected since the residual is zero at equilibrium. Rearranging the remaining terms that depend on the derivative of \mathbf{u} with respect to \hat{x}_e yields

$$\frac{\partial c(\mathbf{u}, \hat{\mathbf{x}})}{\partial \hat{x}_e} = \left(\mathbf{f}_{ext}^T + \boldsymbol{\lambda}^T \frac{\partial \mathbf{r}}{\partial \mathbf{u}} \Big|_{\hat{x}_e=const} \right) \frac{\partial \mathbf{u}}{\partial \hat{x}_e} + \boldsymbol{\lambda}^T \frac{\partial \mathbf{r}}{\partial \hat{x}_e} \Big|_{\mathbf{u}=const}. \quad (3.27)$$

In order to simplify (3.27), the parenthesis on the right-hand side is set to zero, that is,

$$\mathbf{f}_{ext}^T + \boldsymbol{\lambda}^T \frac{\partial \mathbf{r}}{\partial \mathbf{u}} \Big|_{\hat{x}_e=const} = \mathbf{0}. \quad (3.28)$$

The derivatives of the residual are deducted separately for legibility. Deriving the residual \mathbf{r} in (2.46) with respect to \mathbf{u} , considering that \mathbf{f}_{ext} does not depend on \mathbf{u} , yields

$$\begin{aligned} \frac{\partial \mathbf{r}}{\partial \mathbf{u}} \Big|_{\hat{x}_e=const} &= \frac{\partial \mathbf{f}_{ext}}{\partial \mathbf{u}} \Big|_{\hat{x}_e=const} - \frac{\partial \mathbf{f}_{int}}{\partial \mathbf{u}} \Big|_{\hat{x}_e=const} \\ &= -\mathbf{K}_T. \end{aligned} \quad (3.29)$$

where (2.48) was used to further simplify the equation. Likewise, deriving (2.46) with respect to \hat{x}_e yields

$$\begin{aligned} \frac{\partial \mathbf{r}}{\partial \hat{x}_e} \Big|_{\mathbf{u}=const} &= \frac{\partial \mathbf{f}_{ext}}{\partial \hat{x}_e} \Big|_{\mathbf{u}=const} - \frac{\partial \mathbf{f}_{int}}{\partial \hat{x}_e} \Big|_{\mathbf{u}=const} \\ &= -\frac{\partial \mathbf{f}_{int}}{\partial \hat{x}_e} \Big|_{\mathbf{u}=const}. \end{aligned} \quad (3.30)$$

Substituting (3.29) into (3.28) and solving for $\boldsymbol{\lambda}$ yields

$$\boldsymbol{\lambda} = \mathbf{K}_T^{-1} \mathbf{f}_{ext}, \quad (3.31)$$

where the symmetric property of \mathbf{K}_T was invoked. Substituting (3.28) and (3.30) into (3.27) yields:

$$\frac{\partial c(\mathbf{u}, \hat{\mathbf{x}})}{\partial \hat{x}_e} = -\boldsymbol{\lambda}^T \frac{\partial \mathbf{f}_{int}(\mathbf{u}, \hat{\mathbf{x}})}{\partial \hat{x}_e} \Big|_{\mathbf{u}_e = \text{const}}. \quad (3.32)$$

The derivative of the internal force with respect to the \hat{x}_e is derived for each interpolation in the following subsections. Although the contribution \mathbf{f}_e of all elements is necessary to compute \mathbf{f}_{int} , only one element needs to be considered at a time. This is proved in Section 3.3.1, but is not repeated in the following subsections for brevity.

3.3.1

No interpolation (None)

At first, the sensitivity analysis is performed at global level. Substituting (3.11) in (2.52) and deriving it with respect to \hat{x}_e at $e = e^*$ yields

$$\begin{aligned} \frac{\partial \mathbf{f}_{int}}{\partial \hat{x}_e} \Big|_{e=e^*} &= \frac{\partial}{\partial \hat{x}_e} \Big|_{e=e^*} \bigcap_{e=1}^{N_e} \hat{x}_e \mathbf{f}_e^{NL} \\ &= \bigcap_{e=1}^{N_e} \frac{\partial (\hat{x}_e \mathbf{f}_e^{NL})}{\partial \hat{x}_e} \Big|_{e=e^*} \\ &= \bigcap_{e=1}^{N_e} \mathbf{f}_e^{NL} \Big|_{e=e^*} = \bigcap_{e=1}^{N_e} \mathbf{f}_{e^*}^{NL} \end{aligned} \quad (3.33)$$

From (3.33), it follows that only an element e^* is assembled in the derivative with respect to \hat{x}_e at $e = e^*$. For implementation purposes, the derivative of the compliance with respect to \hat{x}_e may be easily computed from equations (3.32) and (3.33) as

$$\frac{\partial c}{\partial \hat{x}_e} = -\boldsymbol{\lambda}_e^T \mathbf{f}_e^{NL} \quad (3.34)$$

where $\boldsymbol{\lambda}_e$ is a vector formed by the adjoint vector's components respective to the degrees of freedom of \mathbf{f}_e^{NL} .

3.3.2

Energy Interpolation

The element's force vector for this case depends implicitly on $\gamma_e(\bar{x}_e)$, so the original equation for the sensitivity should be rewritten from (3.21) and (3.32), the chain rule can be expressed as follows:

$$\frac{\partial c(\mathbf{u}, \mathbf{x})}{\partial x_e} = -\boldsymbol{\lambda}_e^T \frac{d\mathbf{f}_e}{d\bar{x}_e} \frac{\partial \bar{x}_e}{\partial \tilde{x}_e} \frac{\partial \tilde{x}_e}{\partial x_e} \quad (3.35)$$

where the derivative of \mathbf{f}_e with respect to \bar{x}_e should be obtained. To do so, it is necessary to use the chain rule in order to obtain the total derivative of \mathbf{f}_e with respect to \bar{x} (instead of \hat{x}) by deriving (3.16), that is

$$\frac{d\mathbf{f}_e}{d\bar{x}_e} = \frac{\partial \mathbf{f}_e}{\partial \hat{x}_e} \frac{\partial \hat{x}_e}{\partial \bar{x}_e} + \frac{\partial \mathbf{f}_e}{\partial \gamma_e} \frac{\partial \gamma_e}{\partial \bar{x}_e}. \quad (3.36)$$

The first term on the right-hand side is the partial derivative of (3.16) with respect to \hat{x}_e , that is

$$\frac{\partial \mathbf{f}_e}{\partial \hat{x}_e} = \gamma_e \mathbf{f}_e^{NL}(\gamma_e \mathbf{u}_e) + (1 - \gamma_e^2) \mathbf{f}_e^L(\mathbf{u}_e). \quad (3.37)$$

The second term on the right-hand side of (3.36) has already been determined in (3.24). The third term is obtained by deriving (3.16) with respect to γ_e which gives

$$\frac{\partial \mathbf{f}_e}{\partial \gamma_e} = \left[\mathbf{f}_e^{NL}(\gamma_e \mathbf{u}_e) + \gamma_e \frac{\partial \mathbf{f}_e^{NL}(\gamma_e \mathbf{u}_e)}{\partial (\gamma_e \mathbf{u}_e)} \frac{\partial (\gamma_e \mathbf{u}_e)}{\partial \gamma_e} - 2\gamma_e \mathbf{f}_e^L(\mathbf{u}_e) \right] \hat{x}_e. \quad (3.38)$$

The second term from the right-hand side in (3.38) may be simplified from (2.48) as follows:

$$\mathbf{K}_e^{NL}(\gamma_e \mathbf{u}_e) = \frac{\partial \mathbf{f}_e^{NL}(\gamma_e \mathbf{u}_e)}{\partial (\gamma_e \mathbf{u}_e)}. \quad (3.39)$$

The last partial derivative in (3.38) is reduced to

$$\frac{\partial (\gamma_e \mathbf{u}_e)}{\partial \gamma_e} = \mathbf{u}_e. \quad (3.40)$$

Substituting (3.39) and (3.40) into (3.38) gives

$$\frac{\partial \mathbf{f}_e}{\partial \gamma_e} = [\mathbf{f}_e^{NL}(\gamma_e \mathbf{u}_e) + \gamma_e \mathbf{K}_e^{NL}(\gamma_e \mathbf{u}_e) \mathbf{u}_e - 2\gamma_e \mathbf{f}_e^L(\mathbf{u}_e)] \hat{x}_e. \quad (3.41)$$

Unlike the linear case, the product $\mathbf{K}_e^{NL}(\gamma_e \mathbf{u}_e) \gamma_e \mathbf{u}_e$ cannot be simplified to $\mathbf{f}_e^{NL}(\gamma_e \mathbf{u}_e)$. Finally, the last term in (3.36) is obtained by deriving (3.15) with respect to \hat{x}_e , that yields

$$\frac{\partial \gamma_e(\bar{x}_e)}{\partial \bar{x}_e} = \frac{\beta_1 \bar{x}_e^{p-1} \text{sech}^2[\beta_1(\bar{x}_e^p - \rho_0)]}{\tanh(\beta_1 \rho_0) + \tanh[\beta_1(1 - \rho_0)]}. \quad (3.42)$$

3.3.3

Additive Hyperelasticity

The derivative of \mathbf{f}_e with respect to \hat{x}_e is obtained by deriving (3.19) as follows

$$\begin{aligned} \frac{\partial \mathbf{f}_e}{\partial \hat{x}_e} &= \frac{\partial}{\partial \hat{x}_e} [\hat{x}_e \mathbf{f}_e^{NL}(\mathbf{u}_e) + (1 - \hat{x}_e) \mathbf{f}_e^Y(\mathbf{u}_e)] \\ &= \mathbf{f}_e^{NL}(\mathbf{u}_e) - \mathbf{f}_e^Y(\mathbf{u}_e). \end{aligned} \quad (3.43)$$

Similar to (3.34), the derivative of the compliance with respect to \hat{x}_e is obtained by substituting (3.43) in (3.34), which yields

$$\frac{\partial c}{\partial \hat{x}_e} = -\boldsymbol{\lambda}_e^T [\mathbf{f}_e^{NL}(\mathbf{u}_e) - \mathbf{f}_e^Y(\mathbf{u}_e)]. \quad (3.44)$$

3.3.4

Validation of the sensitivity

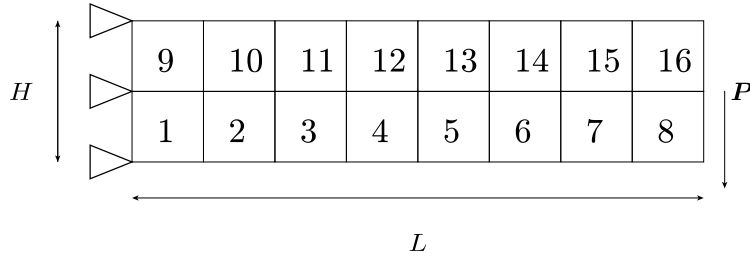
A validation of the sensitivity is presented in this subsection. Each element's design variable is set to an initial value $x_e = x^*$ that is perturbed one element at a time by a factor $\Delta x = 10^{-3}$. The sensitivity components are approximated using Central Finite Differences (CFD) given by the expression

$$\frac{\partial c}{\partial x_e} \approx \frac{c(x_e^* + \Delta x) - c(x_e^* - \Delta x)}{2\Delta x}, \quad (3.45)$$

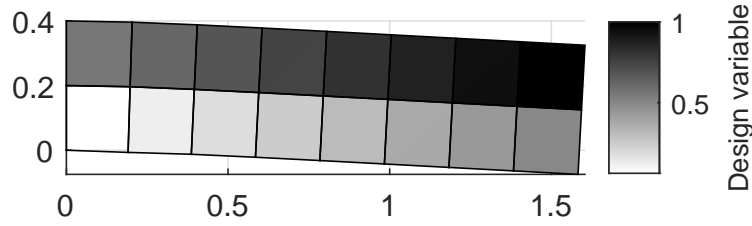
and the maximum relative error given is considered for this analysis using the following approximation:

$$Error \approx \max \left| \frac{dc_A - dc_N}{dc_N} \right| \quad (3.46)$$

where dc_A and dc_N are the sensitivities computed analytically and numerically, respectively. To perform the validation, a common problem in the literature (Chen *et al.*, 2019a, Appendix B, adapted) is used: a unitary thickness cantilever beam subject to a point load on the right edge's central node (see Figure 3.17). The NR tolerance was set to 10^{-6} for all FEA in this section.



3.17(a): Domain meshed with 2x8 Q4 elements.



3.17(b): Deformed beam with design variable in a gray scale.

Figure 3.17: Clamped beam subject to a point load.

Table 3.6: Parameters of the clamped beam problem

Parameter	Value
Material model	W^1
Length (L)	1.6 m
Height (H)	0.4 m
Young modulus (E)	3 GPa
Poisson coefficient (ν)	0.4
Filter radius (r_{min})	0.4
Penalization factor (p)	3
Applied load (P)	25 kN

Each design variable is set to $x_e = e/16$ with $e = 1, \dots, 16$. This choice ensures the filter is effectively considered in the validation and that there are

elements modeled after linear and nonlinear formulations for the EI method. Table 3.6 lists the parameters used in this analysis.

Table 3.7 lists the sensitivities for each element and method, which agree with the values approximated using CFD. The last row of the table is the maximum relative error for each method. It is pointed out that the similarities between the values for no interpolation and AH are due to the term $\mathbf{f}_e^Y(\mathbf{u}_e)$ in (3.44) being too small to presents a significant difference to (3.34).

Table 3.7: Numerical sensitivity analysis for the interpolation methods

e	No interpolation		EI		AH	
	dc_N	dc_A	dc_N	dc_A		
1	$-7.57E3$	$-7.57E3$	$-7.19E3$	$-7.19E3$	$-7.57E3$	$-7.57E3$
2	$-5.77E3$	$-5.77E3$	$-5.45E3$	$-5.45E3$	$-5.77E3$	$-5.77E3$
3	$-1.59E3$	$-1.59E3$	$-1.41E3$	$-1.41E3$	$-1.59E3$	$-1.59E3$
4	-382	-382	-308	-308	-382	-382
5	-101	-101	-103	-103	-101	-101
6	-26.5	-26.5	-26.8	-26.8	-26.5	-26.5
7	-6.87	-6.87	-6.92	-6.92	-6.87	-6.87
8	-1.92	-1.92	-1.92	-1.92	-1.92	-1.92
9	$-9.6E3$	$-9.6E3$	$-8.96E3$	$-8.96E3$	$-9.6E3$	$-9.6E3$
10	$-6.91E3$	$-6.91E3$	$-6.43E3$	$-6.43E3$	$-6.91E3$	$-6.91E3$
11	$-1.76E3$	$-1.76E3$	$-1.6E3$	$-1.6E3$	$-1.76E3$	$-1.76E3$
12	-387	-387	-333	-333	-387	-387
13	-91.5	-91.5	-91.7	-91.7	-91.5	-91.5
14	-22.1	-22.1	-22.1	-22.1	-22.1	-22.1
15	-5.41	-5.41	-5.42	-5.42	-5.41	-5.41
16	-1.44	-1.44	-1.44	-1.44	-1.44	-1.44
Error	$1.0109e - 05$		$9.5371e - 05$		$1.0109e - 05$	

Notice that the greatest relative error is below 0.01% for all methods, so it is considered that the numerical and analytical sensitivities are sufficiently close for a range of design variables' values, including those in transition between linear and nonlinear in the EI method. The validation of the sensitivities' equations is thereby complete.

4

Results and discussions

This chapter is dedicated to comparing the influence of material models and interpolation methods on the topology optimization of two well-known problems in the literature: the cantilever beam and the clamped beam. Although these problems may be analyzed in plane stress condition, they are considered in plane strain in this chapter to enable comparison with other authors.

The optimization procedure detailed in chapter 3 is used to solve these problems, but some techniques were required to help the MMA optimizer converge to an optimal topology. The design variables are set to unity, *i.e.*, $x_e = 1$ for every element, at the start of the optimization.

The penalization factor p is incremented by Δp every few TO iterations, starting at 1 up to 3. The sharpness parameter β is set to 4 initially, but it is updated at the end of the process, as follows:

- For $1 \leq p < 2$: p is updated every 2 iterations;
- For $2 \leq p < 3$: p is updated every 5 iterations;
- For $p = 3$: p is not updated anymore. β is doubled every 10 iterations up to 64.

The increment is $\Delta p = 0.05$ for the cantilever beam and $\Delta p = 0.10$ for the clamped beam. This continuation procedure is based on the original article, used as reference (Wang *et al.*, 2014). To avoid abrupt changes of the design at later stages of the optimization process (*i.e.*, $p = 3$), the update of the design variables is scaled so the maximum change is $\Delta x_{lim} = 0.10$, called the move limit.

The load step is set to 10% of the maximum load by default. However, if the analysis does not converge in 20 iterations (per load step), the step is reduced to 1%.

Since significant displacement is necessary to properly analyze the results considering geometrically nonlinearities, a soft material, Nylon, is used for both problems in this chapter. The material parameters suggested by Buhl *et al.* (2000) are used: $E = 3$ GPa and $\nu = 0.4$. The remaining parameters were computed from (2.23), (2.24), (2.25) and (2.37).

4.1

Comparison of hyperelastic models

The cantilever beam is used here to compare the optimized topologies using the different material models. Wang *et al.* (2014) showed the different optimized topologies obtained using W^1 , W^4 and W^7 . However, that implementation was limited to the use of models whose strain energy densities were proportional to the Young modulus. This work's version of the EI method is used to solve the current problem and is able to handle more general models such as Mooney-Rivlin and Yeoh, as described in Section 3.2.2.

The problem's domain is represented in Figure 4.1, where a thickness $t = 0.1$ m is considered, the filter radius r_{min} is the height divided by 8 and $V_{frac} = 0.5$.

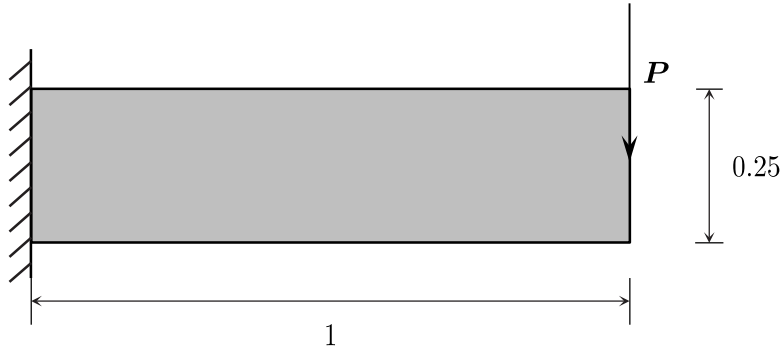
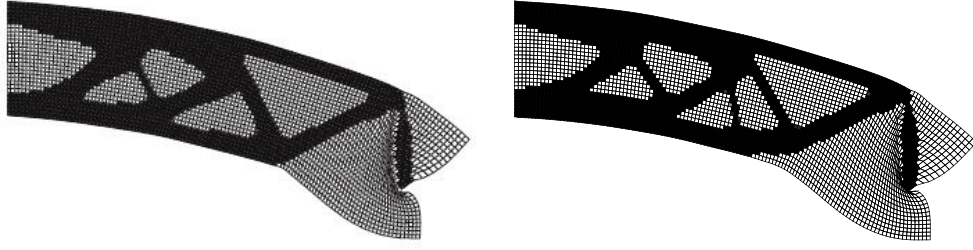
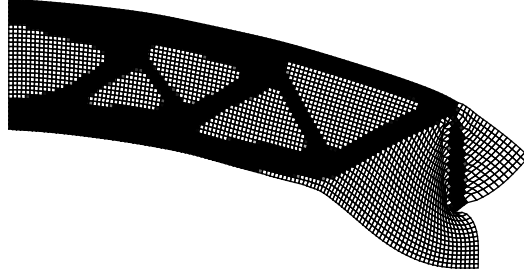


Figure 4.1: Cantilever beam domain, dimensions in meters (Leitão & Pereira, 2019, adapted).

The results shown in this section were calculated for a load $P = 300$ kN and are compared with two different authors who used the standard St. Venant-Kirchhoff model (W^1). Leitão & Pereira (2019) used the Residual Interpolation (RI) proposed by the original author (Wang *et al.*, 2014, Appendix A), which led to a less compliant structure. Figure 4.2 shows the deformed optimized beam obtained by other authors, from which it is notable that qualitatively different designs can be obtained.









4.2(a): Wang *et al.* (2014): $c = 84.94$ kJ. 4.2(b): Leitão & Pereira (2019): $c = 84.83$ kJ.



4.2(c): This work: $c = 84.72$ kJ.

Figure 4.2: Deformed mesh of the optimized cantilever beam using EI from different authors.

Table 4.1: Comparison of optimized topologies for models that use Jacobian terms added to the base SVK and nH. V/V_Ω in parenthesis.

Formulation	St. Venant-Kirchhoff	neo-Hookean
(2.33)	 $W^2: c = 85.74$ kJ (48.3%) [†]	 $W^5: c = 84.89$ kJ (49.5%) [‡]
(2.34)	 $W^3: c = 84.81$ kJ (49.3%)	 $W^6: c = 85.61$ kJ (48.5%) ^{†‡}
(2.35)	 $W^4: c = 84.79$ kJ (49.3%)	 $W^7: c = 86.57$ kJ (48.2%) [†]

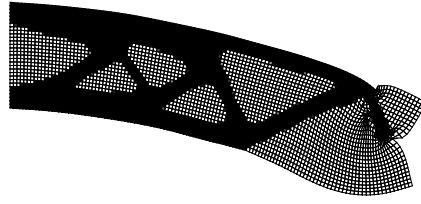
[†] Results for $\beta = 32$;

[‡] Δx_{lim} set to 0.2 at $p = 2.5$ and step size reduced to 0.5%.

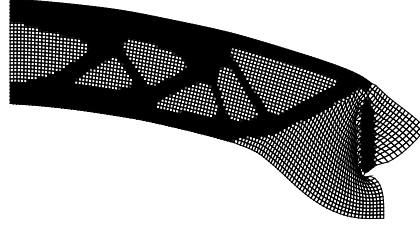
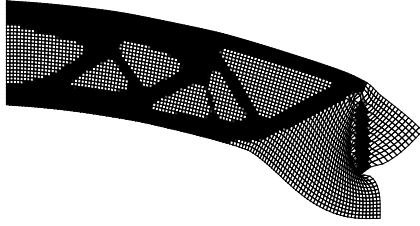
Table 4.1 shows the optimized structures for the models with Jacobian

terms defined in Section 2.1.4 applied to SVK and nH base models. In some cases where $\beta = 64$ led to convergence difficulties or generated an undesirable topology, a previous result was used. Alterations to the move limit and further reductions of the minimum step size were also implemented as shown in the table.

Tests have shown that, for the set of optimization parameters chosen, $\beta = 64$ is a higher end value than desirable in some cases: Figure 4.3(a) shows an anomalous deformation of the “tip” of the beam; Figures 4.3(b) and 4.3(c) depicts topologies where the “tip” of the beam is connected to the rest of the structure by low-density elements.



4.3(a): W^2 : $c = 59.2216$ kJ (49.4%).

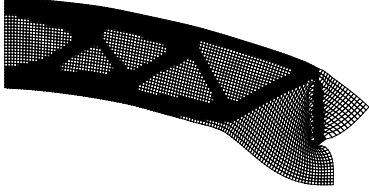
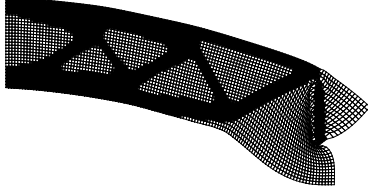
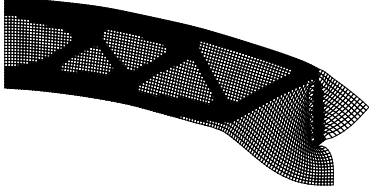
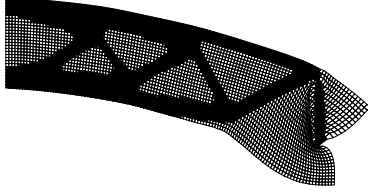
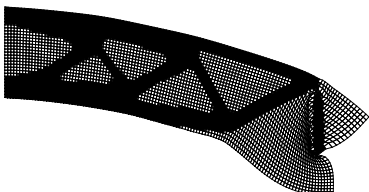
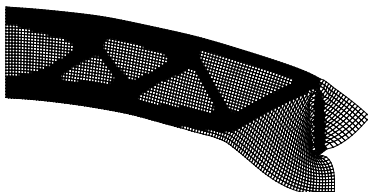


4.3(b): W^6 : $c = 86.9761$ kJ (49.1%). 4.3(c): W^7 : $c = 86.5410$ kJ (48.9%).

Figure 4.3: Undesirable topologies obtained at $\beta = 64$. V/V_Ω in parenthesis.

The topology obtained in Figure 4.2(c) is the least compliant, and is analyzed with the models in Table 4.1. The results are shown in Table 4.2, where all the compliance values were similar. With the exception of W^4 and W^5 , every model has shown better performance compared to its respective previous result. These discrepancies were also observed by Wang *et al.* (2014) and are due to the difficulties of fine-tuning the optimization process for highly nonlinear problems.

Table 4.2: Deformed structures for models that use Jacobian terms added to SVK and nH using the topology from Figure 4.2(c). $V/V_\Omega = 49.2\%$ for every case.

Added term	St. Venant-Kirchhoff	neo-Hookean
(2.33)	 $W^2 : c = 84.77 \text{ kJ}$	 $W^5 : c = 85.49 \text{ kJ}$
(2.34)	 $W^3 : c = 84.78 \text{ kJ}$	 $W^6 : c = 85.48 \text{ kJ}$
(2.35)	 $W^4 : c = 84.81 \text{ kJ}$	 $W^7 : c = 85.46 \text{ kJ}$

It can be observed from Table 4.2 that the use of hyperelastic models did not seem to significantly influence the end design, as the differences found between the results seem to be due to the optimization method itself rather than the material used. Wang *et al.* (2014) has attributed this to the fact that the strain in most elements is between 0.8 and 1.2, a range where the chosen models behave very similarly to each other (see Figure 2.1).

The cantilever beam has been optimized with nearly incompressible Mooney-Rivlin and Yeoh models, *i.e.*, W^8 and W^9 . The parameters used for this analysis were defined as follows: the bulk modulus was calculated from (2.25), the compressibility constants were set to $D_1 = D_2 = 2/K$, and the remaining constants were set to the same value $A_{10} = A_{01} = A_{20} = \mu/2$.

4.4(a): W^8 : $c = 52.19$ kJ (49.4 %).4.4(b): W^9 : $c = 85.12$ kJ (49.5 %).

Figure 4.4: Optimized cantilever beam using Mooney-Rivlin and Yeoh models and their compliances. V/V_Ω in parenthesis.

As described in Chapter 3, the proposed approach of penalizing the strain energy density instead of the material's parameters works for a general hyperelastic model, depicted in Figure 4.4. The topology found using W^8 in Figure 4.4(a) is significantly different than the others presented so far in this chapter. Since $A_{10} = A_{01} = \mu/2$ were chosen, from (2.24) and (2.37), it follows that this material's Young modulus is effectively twice as much as the others, thus the less compliant solution.

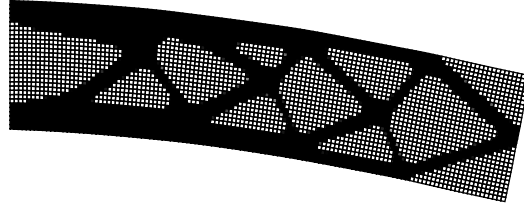
Furthermore, the compliance for the topology in Figure 4.4(b) is close to previous results shown in this work, further confirming that the use of hyperelastic models does not seem to significantly affect this benchmark problem's results. Let it be noted that the use of more complex models can influence computing time, since the tangent stiffness matrix may take longer to compute depending on the complexity of the constitutive tensor.

4.2

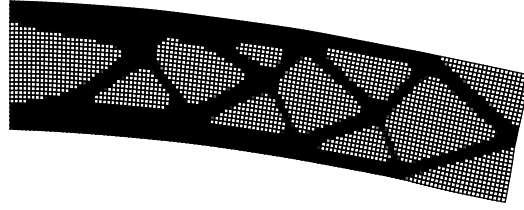
Comparison of interpolation methods

The cantilever problem is considered again using W^1 model with the interpolation methods presented in this thesis: None, EI and AH. The applied load P for this problem is usually set to 144, 240 and 300 kN in the literature (Leitão & Pereira, 2019; Wang *et al.*, 2014; Lahuerta *et al.*, 2013). Even though the EI method was able to converge for higher loads, the other two did not converge for $P = 240$ kN or higher within 200 NR iterations (per load step) even when reducing the stepsize to 0.05 % (which corresponds to 1.2 kN). Thus the results shown are for $P = 144$ kN, the highest value for which every method converged.

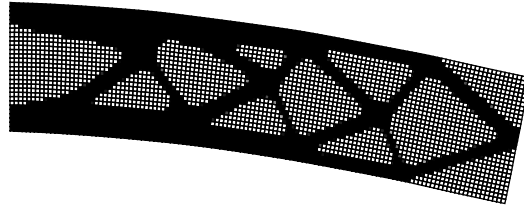
The procedures presented at the start of the chapter were used, except for the initial load step which was considered to be 100 % of the applied load, reduced to 1 % when it did not converge in 20 NR iterations.



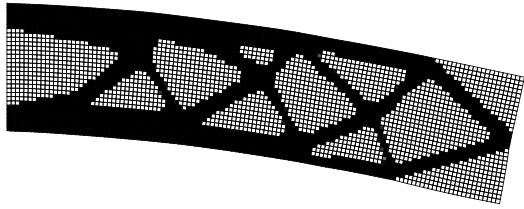
4.5(a): None ($c = 20.87$ kJ).



4.5(b): Energy interpolation ($c = 20.90$ kJ).



4.5(c): Additive hyperelasticity ($c = 20.87$ kJ).



4.5(d): Residual interpolation (Leitão & Pereira (2019)) ($c = 20.88$ kJ).

Figure 4.5: Deformed optimized cantilever beam for $P = 144$ kN with different interpolation methods. End-compliance values in parenthesis.

Figure 4.5 shows the topologies obtained using the different methods, and the results show that they all converged to a similar topology and end-compliance value.

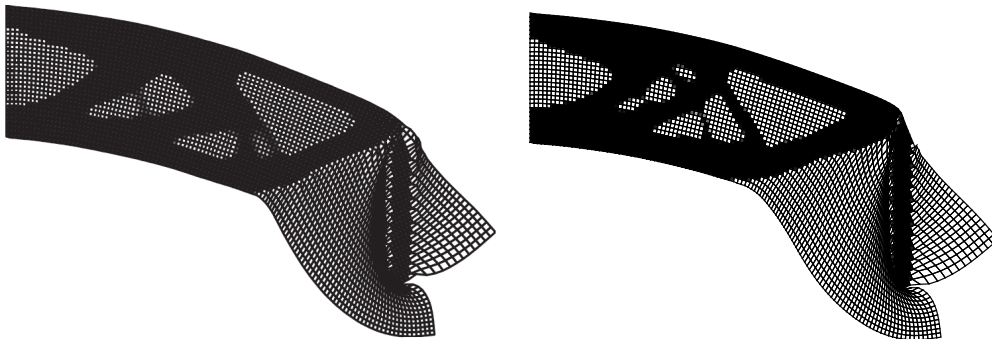
Table 4.3: Performance of interpolation methods for the results shown in Figures 4.5(a) to 4.5(c).

Method	Compliance (kJ)	V/V_Ω (%)	NR iterations	Time (s)
None	20.8750	49.7	523	589
EI	20.9029	49.6	524	754
AH	20.8750	49.6	523	2245

The performance of the interpolation methods is analyzed from the metrics shown in Table 4.3, where the computing time was calculated using the functions *tic* and *toc*, as recommended by MATLAB's documentation, but should be considered as rough estimates. The version of MATLAB is R2019b and specifications of the computer used in this analysis are as follows: Intel Core i7 4790s at 3.20 GHz and 12 GB DDR3 of RAM.

All methods performed similarly in every aspect, except for the elapsed time, for which using no interpolation has performed best. This is due to the extra cost required to compute the contribution of linear and Yeoh models in EI and AH methods, respectively. It is noted that the extra cost of the linear models in EI could be removed by computing the matrices K_e^L in (3.17) on the first time the FEA is performed, and stored for the subsequent analyses.

Given that even the case with no interpolation converged with a single unitary load step, no significant improvement is observed by using an interpolation method. On the other hand, the EI method has converged for P up to 500 kN in this work and Wang *et al.* (2014) (see Figure 4.6(a)). The following changes were implemented to ensure convergence in the result presented in Figure 4.6(b): $\beta_1 = 200$, $\epsilon = 10^{-4}$ and the parameter c_1 in (3.3a) was set to 10^9 .



4.6(a): Wang *et al.* (2014) ($c = 204.534$ kJ). 4.6(b): This work ($c = 204.445$ kJ).

Figure 4.6: Deformed optimized cantilever beam for $P = 500$ kN using EI and W^1 . End-compliance values in parenthesis.

4.3

Clamped beam

The clamped beam problem is considered to compare the performance of the interpolation methods. It is known that the optimized topology for a 10% volume restriction using the linear formulation is drastically different than the one obtained for higher loads in nonlinear analysis, which will be shown throughout this section. The problem's domain is shown in Figure 4.7, where the thickness of the beam is $t = 0.1$ m and the black square represents a region of 2 by 2 elements where the load is evenly divided to better distribute it. The mesh is composed of 120 by 40 Q4 elements that are fixed on the left and right edges, $r_{min} = 0.05$ m and $V_{frac} = 0.1$.

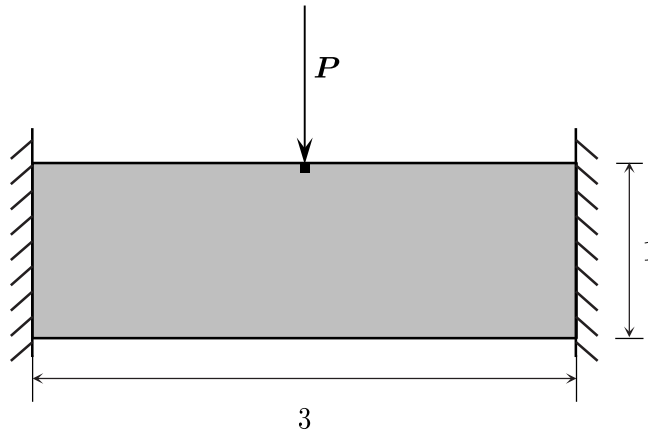
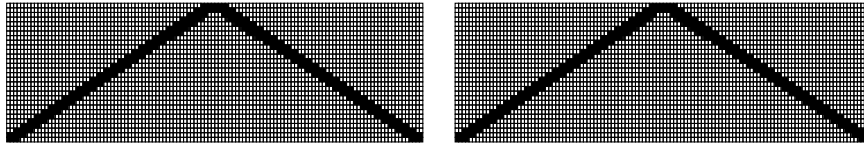


Figure 4.7: Clamped beam domain, dimensions in meters (Leitão & Pereira, 2019, adapted).

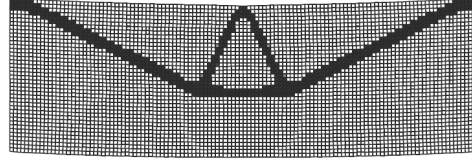
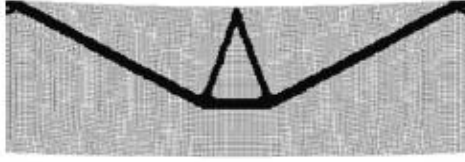
The standard procedure described at the start of this chapter was able to lead to an optimum using all methods for smaller loads. Due to the similarities in results between using no interpolation and AH, only the latter is compared to EI method in Figure 4.8.



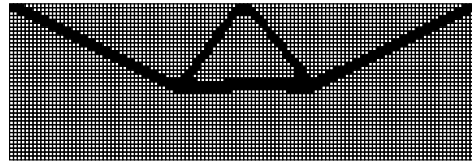
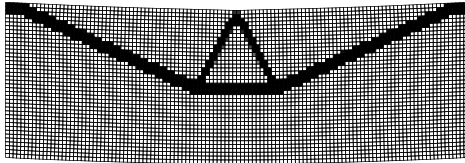
4.8(a): Energy Interpolation ($c = 280.867$ J and $V/V_{\Omega} = 9.96$ %). 4.8(b): Additive Hyperelasticity ($c = 297.738$ J and $V/V_{\Omega} = 9.67$ %).

Figure 4.8: Optimized topology for $P = 50$ kN using two interpolation methods. End-compliance and V/V_{Ω} in parenthesis.

The optimal topology is significantly different for high loadings due to buckling effects. By using $\beta_1 = 100$ and $\epsilon = 10^{-4}$, the problem could be solved for $P = 230$ kN, as shown in Figure 4.9.



4.9(a): Lahuerta *et al.* (2013) ($c = 13.290$ kJ). 4.9(b): Wang *et al.* (2014) ($c = 11.368$ kJ).



4.9(c): Leitão & Pereira (2019) ($c = 11.945$ kJ). 4.9(d): This work ($c = 11.503$ kJ).

Figure 4.9: Optimized topology for $P = 230$ kN with different interpolation methods. W^1 in plane strain was used in every case. End-compliance values in parenthesis.

4.4

Final remarks

The TO process is very reliant on the fine tuning of techniques, including, but not limited to: types of filter, projection and penalization, continuation parameters, and load steps. It is possible to make all methods converge for even higher applied loads by adjusting these factors and the load step, at the cost of possibly unreasonably increasing the time taken to optimize a structure.

It is noted that the AH method has been designed specifically to work in plane stress Luo *et al.* (2015) with an update scheme, and its shortcomings are due to unrealistic behavior of the additive nearly incompressible Yeoh material in plane strain under significant compression. Still, a proper implementation of the update scheme in plane strain should lead to more promising results.

5

Conclusion

A theoretical and practical comparison of interpolation methods that formulate the low-density elements using a lower stiffness material has been presented in this work, alongside the use of different hyperelastic models. However, little numerical and topological differences were found in the benchmark problems using different material models.

Two C-shape problems were analyzed: the former was used to investigate the influence of the hyperelastic parameter A_{20} on the convergence of the analysis using the AH method in plane strain; the latter compared the interpolation methods and showed the behavior of the low-density elements under high compression, from which it has been found that the AH method does not provide as smooth results as the EI method. Moreover, it is possible that any model that provides resistance to compression could be improper to model low-density elements in plane strain, due to the undesirable behavior of the void region under compression. However, it is noted that these results were obtained for plane strain problems, while the AH method was originally intended to work in plane stress with an update scheme of the Yeoh model's parameters, which was not successfully implemented in this work.

The optimization algorithm used has been able to converge to optimized designs of the cantilever beam using different materials and interpolations. However, the continuation procedures and parameters were very sensitive to change and could be improved with further investigation. Thus, even though convergence was achieved, some cases required adjusting parameters such as the move limit and the Ersatz stiffness.

The EI method was able to converge for much higher loads than the case with no interpolation at the cost of extra computational time. A proper implementation of the AH method to plane strain could present better results or solve more difficult problems, however, the arguably simpler and more robust implementation of the EI method has been preferred by some authors (cited in the Introduction of this work) and found success.

5.1

Suggestions for future works

To further extend this research field, a few suggestions are made in this section, from problems that could not be directly addressed in this thesis. First, implementing the interpolation methods to three dimensions would help determine whether AH could be useful outside plane stress.

The use of optimization algorithms (other than MMA and OC) and continuation procedures may be investigated, since the proper adjustment of these processes may greatly enhance the robustness of the TO.

The update scheme originally introduced for the AH by Luo *et al.* (2015) could be adapted to better work in plane strain. Chen *et al.* (2019a) used an equivalent logarithmic strain for the update scheme instead of the von Mises strain used originally, so further investigation on the influence of this choice could be made. Furthermore, the use of a logarithmic strain measure to define a material model could be useful for applications with large displacements and deformations.

5.1.1

Update scheme for Additive Hyperelasticity in plane strain

An adaptation of the update scheme proposed by Luo *et al.* (2015) is suggested for future works: A_{20} is computed at the start of every TO iteration k according to the following criterion

$$A_{20}^{(k)} = \begin{cases} \max \left(\sqrt{\frac{E_{\text{von}}^{(k-1)}}{E^*}}, 0.8 \right) \cdot A_{20}^{(k-1)}, & \text{if } E_{\text{von}}^{(k-1)} \leq E^* \\ \left(\frac{E_{\text{von}}^{(k-1)}}{E^*} \right)^2 \cdot A_{20}^{(k-1)}, & \text{if } E_{\text{von}}^{(k-1)} > E^* \end{cases} \quad (5.1)$$

where E^* is a reference strain value set to 1.2. E_{von} is the maximal von Mises (equivalent) strain given by

$$E_{\text{von}} = \max_e \left(\sqrt{\frac{2}{3} \mathbf{E}_e^{\text{dev}} : \mathbf{E}_e^{\text{dev}}} \right) \quad (5.2)$$

and $\mathbf{E}_e^{\text{dev}}$ is the deviatoric part of the strain tensor of the e -th element computed from

$$\mathbf{E}_e^{\text{dev}} = \mathbf{E}_e^{\text{GP}} - \frac{1}{3}\text{tr}(\mathbf{E}_e^{\text{GP}})\mathbf{I}. \quad (5.3)$$

The components of \mathbf{E}_e^{GP} are the average of those computed at each Gauss point in element e . Notice from (5.1) that if the maximal strain at a TO iteration is smaller than the reference E^* , the parameter A_{20} is reduced to diminish the error introduced by the additive material, whereas if the strain is higher than E^* , A_{20} is increased to strengthen the material and suppress local instability (Chen *et al.*, 2019a). This parameter is $A_{20,\text{ini}} = 10^{-4}E$ at the start of the TO procedure and is limited by the lower boundary $A_{20,\text{min}} = 10^{-5}E$.

It is noted that some of the aforementioned parameters may need to be adjusted. Furthermore it is yet to be verified whether an update scheme for the compressibility parameters D_i should also be implemented to applications outside plane stress.

Bibliography

- Bathe, KJ. 2014. *Finite element procedures*. 2nd edn. Watertown, MA: Klaus-Jurgen Bathe.
- Bendsøe, Martin Philip. 1989. Optimal shape design as a material distribution problem. *Structural optimization*, 1(4), 193–202.
- Bendsøe, Martin Philip, & Kikuchi, Noboru. 1988. Generating optimal topologies in structural design using a homogenization method. *Computer methods in applied mechanics and engineering*, 71(2), 197–224.
- Bendsøe, Martin Philip, & Sigmund, Ole. 2002. *Topology optimization: theory, methods, and applications*. 2nd edn. Berlin, Brandenburg: Springer Science & Business Media.
- Bonet, Javier, & Wood, Richard D. 2008. *Nonlinear continuum mechanics for finite element analysis*. 2nd edn. Cambridge, Cambridgeshire: Cambridge university press.
- Brink, Ulrich, & Stein, Erwin. 1996. On some mixed finite element methods for incompressible and nearly incompressible finite elasticity. *Computational Mechanics*, 19(1), 105–119.
- Bruns, Tyler, & Tortorelli, Daniel. 1998. Topology optimization of geometrically nonlinear structures and compliant mechanisms. *Page 4950 of: 7th AIAA/USAF/NASA/ISSMO Symposium on Multidisciplinary Analysis and Optimization*.
- Bruns, Tyler E, & Tortorelli, Daniel A. 2001. Topology optimization of non-linear elastic structures and compliant mechanisms. *Computer methods in applied mechanics and engineering*, 190(26-27), 3443–3459.
- Bruns, Tyler E, & Tortorelli, Daniel A. 2003. An element removal and reintroduction strategy for the topology optimization of structures and compliant mechanisms. *International journal for numerical methods in engineering*, 57(10), 1413–1430.

- Buhl, T., Pedersen, C.B.W., & Sigmund, O. 2000. Stiffness design of geometrically nonlinear structures using topology optimization. *Structural and Multidisciplinary Optimization*, 19(2), 93–104.
- Chen, Qi, Zhang, Xianmin, & Zhu, Benliang. 2019a. A 213-line topology optimization code for geometrically nonlinear structures. *Structural and Multidisciplinary Optimization*, 59(5), 1863–1879.
- Chen, Qi, Zhang, Xianmin, Zhang, Hongchuan, Zhu, Benliang, & Chen, Bicheng. 2019b. Topology optimization of bistable mechanisms with maximized differences between switching forces in forward and backward direction. *Mechanism and Machine Theory*, 139, 131–143.
- Crisfield, Michael A. 1981. A fast incremental/iterative solution procedure that handles “snap-through”. *Computational Methods in Nonlinear Structural and Solid Mechanics*, 55–62.
- Curnier, Alain. 1994. *Computational methods in solid mechanics*. 1994th edn. Vol. 29. Dordrecht, The Netherlands: Kluwer Academic Publishers.
- Dassault, Systèmes. 2007. Abaqus analysis user's manual. *Simulia Corp. Providence, RI, USA*.
- Dassault, Systèmes. 2010. *Abaqus Benchmark Manual, Version 6.10*.
- Frecker, M. I., Ananthasuresh, G. K., Nishiwaki, S., Kikuchi, N., & Kota, S. 1997. Topological Synthesis of Compliant Mechanisms Using Multi-Criteria Optimization. *Journal of Mechanical Design*, 119(2), 238–245.
- Gurtin, Morton E. 1981. *An introduction to continuum mechanics*. 1st edn. New York, NY: Academic press.
- Holzappel, A Gerhard. 2000. *Nonlinear solid mechanics*. 1st edn. Chichester, West Sussex: Wiley.
- Huang, X, Zhou, SW, Xie, YM, & Li, Q. 2013. Topology optimization of microstructures of cellular materials and composites for macrostructures. *Computational Materials Science*, 67, 397–407.
- James, Kai A, & Waisman, Haim. 2016. Layout design of a bi-stable cardiovascular stent using topology optimization. *Computer Methods in Applied Mechanics and Engineering*, 305, 869–890.
- Jie, HOU, Xiaojun, GU, Jihong, ZHU, Jie, WANG, & Zhang, Weihong. 2020. Topology optimization of joint load control with geometrical nonlinearity. *Chinese Journal of Aeronautics*, 33(1), 372–382.

- Kawamoto, Atsushi. 2009. Stabilization of geometrically nonlinear topology optimization by the Levenberg–Marquardt method. *Structural and Multidisciplinary Optimization*, **37**(4), 429–433.
- Kim, Nam-Ho. 2014. *Introduction to nonlinear finite element analysis*. 2015th edn. New York, NY: Springer Science & Business Media.
- Klarbring, Anders, & Strömberg, Niclas. 2013. Topology optimization of hyperelastic bodies including non-zero prescribed displacements. *Structural and Multidisciplinary Optimization*, **47**(1), 37–48.
- Lahuerta, Ricardo Doll, Simões, Eduardo T, Campello, Eduardo MB, Pimenta, Paulo M, & Silva, Emilio CN. 2013. Towards the stabilization of the low density elements in topology optimization with large deformation. *Computational Mechanics*, **52**(4), 779–797.
- Lazarov, Boyan Stefanov, Schevenels, Mattias, & Sigmund, Ole. 2011. Robust design of large-displacement compliant mechanisms. *Mechanical sciences*, **2**(2), 175–182.
- Leitão, André Xavier. 2019. *Topology Optimization of Geometrically Nonlinear Structures Based on an Energy Interpolation Scheme*. M.Phil. thesis, Pontifical Catholic University of Rio de Janeiro (PUC-Rio).
- Leitão, André, & Pereira, Anderson. 2019. Topology Optimization of Geometrically Nonlinear Structures Considering an Energy Interpolation Scheme. In: *Proceedings of 25th ABCM International Congress of Mechanical Engineering*, DOI: 10.26678/ABCM.COBEM2019.COB2019-1580.
- Liu, Jikai, Gaynor, Andrew T, Chen, Shikui, Kang, Zhan, Suresh, Krishnan, Takezawa, Akihiro, Li, Lei, Kato, Junji, Tang, Jinyuan, Wang, Charlie CL, et al. . 2018. Current and future trends in topology optimization for additive manufacturing. *Structural and Multidisciplinary Optimization*, **57**(6), 2457–2483.
- Luo, Quantian, & Tong, Liyong. 2016. An algorithm for eradicating the effects of void elements on structural topology optimization for nonlinear compliance. *Structural and Multidisciplinary Optimization*, **53**(4), 695–714.
- Luo, Yangjun, Wang, Michael Yu, & Kang, Zhan. 2015. Topology optimization of geometrically nonlinear structures based on an additive hyperelasticity technique. *Computer methods in applied mechanics and engineering*, **286**, 422–441.

- Mase, G Thomas, Smelser, Ronald E, & Mase, George E. 1999. *Continuum mechanics for engineers*. 2nd edn. Boca Raton, Fl: CRC press.
- Pedersen, C.B.W., Buhl, T., & Sigmund, O. 2001. Topology synthesis of large-displacement compliant mechanisms. *International journal for numerical methods in engineering*, 50(12), 2683–2705.
- Simo, Juan-Carlos, & Armero, Francisco. 1992. Geometrically non-linear enhanced strain mixed methods and the method of incompatible modes. *International Journal for Numerical Methods in Engineering*, 33(7), 1413–1449.
- Suchocki, Cyprian, & Jemioło, Stanisław. 2019. On Finite Element Implementation of Polyconvex Incompressible Hyperelasticity: Theory, Coding and Applications. *International Journal of Computational Methods*, 1950049–1–1950049–31.
- Svanberg, K. 2007. MMA and GCMMA - two methods for nonlinear optimization. *Optimization and Systems Theory, Department of Mathematics. KTH - Royal Institute of Technology in Stockholm, Sweden*, 1–16.
- Svanberg, Krister. 1987. The method of moving asymptotes - a new method for structural optimization. *International journal for numerical methods in engineering*, 24(2), 359–373.
- Talischí, Cameron, Paulino, Glaucio H, Pereira, Anderson, & Menezes, Ivan FM. 2012. PolyTop: a Matlab implementation of a general topology optimization framework using unstructured polygonal finite element meshes. *Structural and Multidisciplinary Optimization*, 45(3), 329–357.
- van Dijk, Nico P, Langelaar, M, & van Keulen, F. 2014. Element deformation scaling for robust geometrically nonlinear analyses in topology optimization. *Structural and Multidisciplinary Optimization*, 50(4), 537–560.
- Wallin, Mathias, Ivarsson, Niklas, & Tortorelli, Daniel. 2018. Stiffness optimization of non-linear elastic structures. *Computer Methods in Applied Mechanics and Engineering*, 330, 292–307.
- Wang, Fengwen, Lazarov, Boyan Stefanov, & Sigmund, Ole. 2011. On projection methods, convergence and robust formulations in topology optimization. *Structural and Multidisciplinary Optimization*, 43(6), 767–784.
- Wang, Fengwen, Lazarov, Boyan Stefanov, Sigmund, Ole, & Jensen, Jakob Sørensgaard. 2014. Interpolation scheme for fictitious domain techniques and topology optimization of finite strain elastic problems. *Computer Methods in Applied Mechanics and Engineering*, 276, 453–472.

- Yoon, Gil Ho, & Kim, Yoon Young. 2005. Element connectivity parameterization for topology optimization of geometrically nonlinear structures. *International journal of solids and structures*, 42(7), 1983–2009.
- Zhang, Xiaojia, Ramos, Adeildo S, & Paulino, Glaucio H. 2017. Material nonlinear topology optimization using the ground structure method with a discrete filtering scheme. *Structural and Multidisciplinary Optimization*, 55(6), 2045–2072.
- Zienkiewicz, Olek C, Taylor, Robert L, & Zhu, Jian Z. 2005. *The finite element method: its basis and fundamentals*. 6th edn. Amsterdam, North Holland: Elsevier Butterworth-Heinemann.